

Development of a Modular Interactive Planet Simulator

Kläre Cassirer , Klaus Fraedrich*, Heiko Jansen*, Wolfgang Joppich ,
Michael Kürschner , Edilbert Kirk*, Marc Lob , Ute Luksch*, Frank Lunkeit*,
Lars Pesch , Sabine Pott , Michael Preuhs , Ulrich Trottenberg

*Meteorological Institute, University of Hamburg
Bundesstr. 55, D-20146 Hamburg, Germany
email: Edilbert.Kirk@dkrz.de

Fraunhofer Institute for Algorithms and Scientific Computing (SCAI)
Schloss Birlinghoven
D-53754 Sankt Augustin, Germany
email: Wolfgang.Joppich@gmd.de

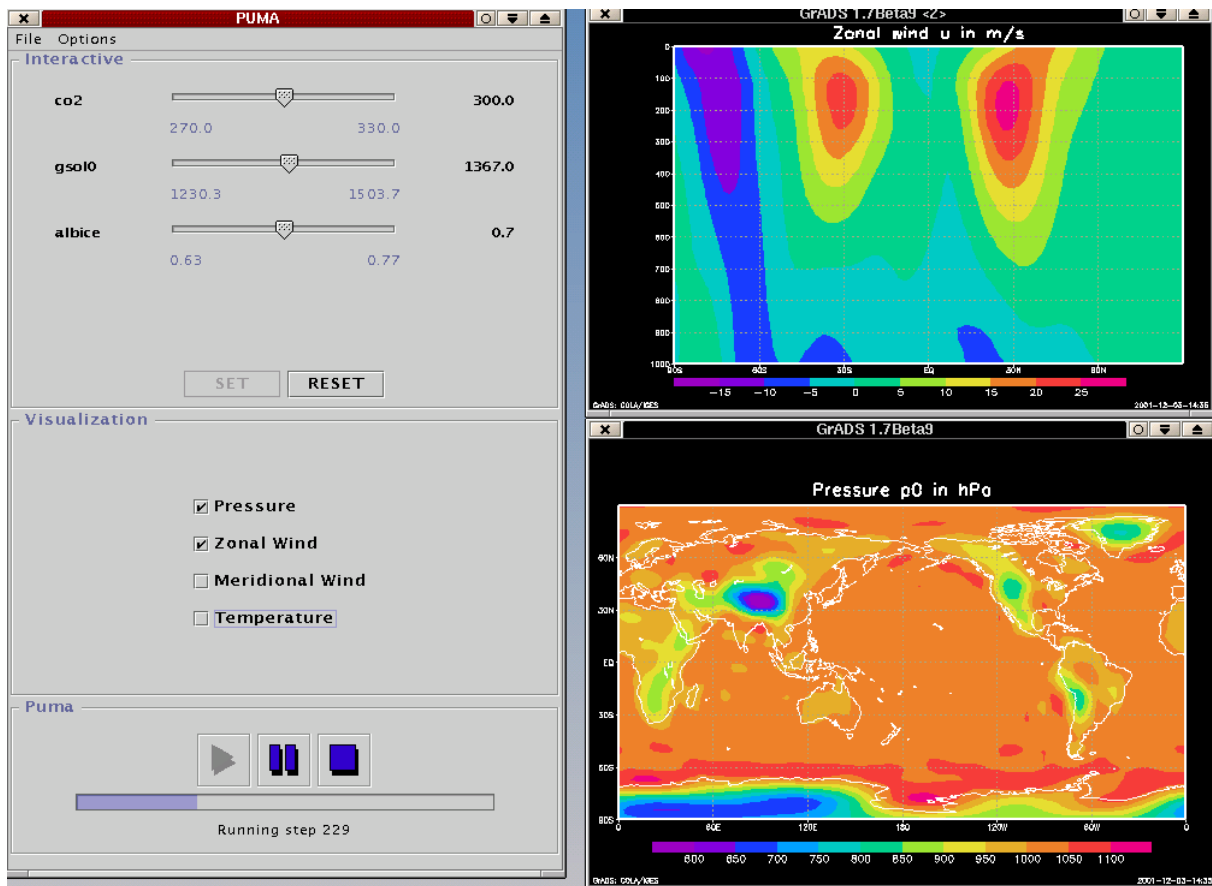


Fig.: 1 Screenshot of Planet Simulator in interactive mode

The **Planet Simulator** is designed as an EMIC (Earth Models of Intermediate Complexity) model, with its priorities set to performance, ease of use, and modularity. The Planet Simulator are:

Modular approach: The code is split into modules, which can be independent from other modules. Where applicable there are different purposes, e.g. ocean models of different complexity or different hardware, e.g. parallel scalar machines versus vector processor machines. Modularity is either on code level (FORTRAN) or on larger components with an coupling interface (MPCCI).

Interaction: The planet simulator can run in basically two modes which don't require any parameter changes during the run. The interactive mode provides the user with a set of controls (sliders, buttons, menus), that have a direct effect on the running model. The interactive mode is designed to aid in applications are education and online visualization of climate experiments.

Portability: The development process is done and tested on different systems. Current development platforms include Cray vector machines, Linux-PCs and Linux-cluster with up to 1000 processors. MPI (Message Passing Interface) is used for multiprocessor and the modules is strict FORTRAN-90 code, avoiding any vendor specific constructs or libraries.

Readability: Though optimized for performance, the code is written so that a student can learn the structure and organization very fast. This leads to makes the planet simulator an ideal training tool for comprehensive models later.

Scalability: The model can be run on selectable resolutions, for each of its larger components like atmosphere, ocean, ice, depending on the need for fast processing or high resolution.

Status: The atmospheric component of the planet simulator is the MOM-3 (1998), while the ocean component is MOM-3. Ice- and vegetation components are under development, while more components will be introduced during the next two years.

Availability: The planet simulator and its source code will be freely available at the end of 2003. Scientist, that participate in the development process have permanent access to the sources of the planet simulator. The atmosphere many tools can be downloaded from our website "<http://puma.dkrz.de/puma>".

Acknowledgement: The project planet simulator is funded by the BMFT at grant 01LG9903.

References:

Becker-Lemgau, U., M. G. Hackenberg, W. Joppich, S. M. Sontowski, and R. Tilch, Solution of Coupled Problems by Parallel Multigrid, the International FORTWIHR Conference 1998 -- High Performance Computing

Computing, Springer Lecture Notes in Computer Science and Engineering, 1998.

Fraedrich, Fraedrich, K., Fraedrich, K., E. Kirk, and F. Lunkeit, 1998: PUMA: Portable University Model for the Atmosphere. DKRZ Technical Report No. 16, DKRZ-Hamburg, 37pp.

High versus Variable Resolution in Climate Modelling

M. Déqué and A.L. Gibelin
Météo-France, CNRM, Toulouse
e-mail: deque@meteo.fr

The ARPEGE/IFS-based climate model in use at Météo-France for about 10 years (Déqué et al., 1994) has a regional version centered over the Mediterranean basin. This version is a spectral global model with variable resolution based on Courtier and Geleyn (1988). Variable resolution over the globe is an alternative to limited area modelling. It demands more to the computer, since about 50% of the calculations are made outside the area of interest, and less to people in charge of the simulation, since the handling of lateral boundary conditions is avoided. Two possible drawbacks arise from this approach. The first one is the impact of variable mesh on the discretization. This drawback is harmless because two neighbouring grid points have a very similar grid spacing, and the error due to the not exact centering of finite differences is negligible compared with the discretization error. The latitude-longitude discretization of most GCMs induces a larger variability in the mesh size as latitude increases. Moreover, when a GCM uses a spectral resolution, this problem disappears. The second drawback is more serious. It is well known that model systematic errors are resolution dependent. There is a risk that systematic errors in the low-resolution part of the globe contaminate the domain of interest. It is even possible that an imbalance between two regions creates an artificial circulation, resulting in a variable resolution model climate poorer than the low resolution model climate.

The variable resolution approach has thus been extensively tested. First tests with an adiabatic formulation have been followed by tests in long climate runs with variable resolution (Déqué and Piedelievre, 1995). It has been demonstrated that at constant computational cost, a variable resolution model over Europe performs better than a constant resolution one. Recently, Lorant and Royer (2001) extended this conclusion to the equatorial domain, using an aquaplanet version of the model.

The capacity of the last generation of computer have made possible the ultimate test, i.e. the comparison of a variable resolution version, with a version with the maximum resolution over the globe. Our variable resolution model has a maximum resolution of 0.5° in the Mediterranean sea, and a minimum resolution of 4.5° in the south Pacific. The challenger version has a 0.5° resolution over the globe. Its cost is 16 times the cost of the variable resolution version in computation time, since the time step must be halved for numerical stability. The memory and storage costs are 9 times that of the variable resolution model. Of course, if one is interested in other regions like the tropics, the high resolution model offers additional advantages versus the « Mediterranean » model.

Both high and variable resolution models have been run 10 years with climatological sea surface temperatures. In these simulations both models use the same time step (15 min) to ensure a clean comparison. A third simulation of the same kind has been performed with the standard version of the climate model (2.8° resolution). The question is whether the variable resolution (VR) produces a climate closer to the high resolution (HR) than the low resolution (LR) in the Mediterranean area. We limit here our analysis to winter (DJF) and summer (JJA) and to 2 m-temperature and precipitation fields. To avoid a trivial result for temperature, this field is corrected from the orography effect with a 6.5 K/km vertical gradient. Indeed VR has a good representation of orography in the high resolution area.

Figure 1 shows the spatial correlation between VR and HR and between LR and HR for winter precipitation and elevation-corrected temperature as a function of the distance from the pole of resolution. As far as temperature is concerned, the correspondance is very good, due to the pole-to-equator temperature gradient. Beyond 4000 km, VR and LR are equally correlated to HR. As far as precipitation is concerned, the correlation is smaller, but VR is a better approximation to HR than LR in the high resolution area.

Figure 2 presents the same parameters for summer. The main difference with winter is in the higher variability of the precipitation correlation as a function of distance. At about 3000 km from the center of the Mediterranean sea, VR exhibits a minimum correlation, due to the differences in precipitation pattern in tropical Africa. Nevertheless, VR is still the better simulator of HR in the high resolution area.

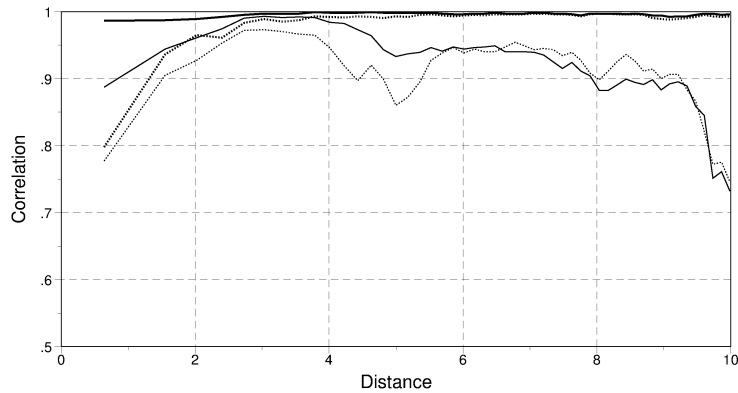


Figure 1: correlation between variable and high resolution (solid line) and between low and high resolution (dot line) as a function of the distance from the center of the Mediterranean sea (unit 1000 km) for precipitation (thin line) and temperature (thick line) in DJF.

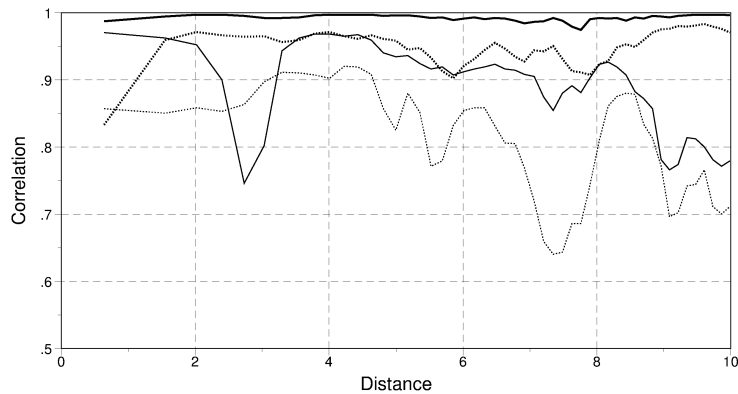


Figure 2: as Figure 1 for JJA.

References

- Courtier, P., and Geleyn, J.F., 1988. A global numerical weather prediction model with variable resolution : application to shallow-water equations. *Quart. J. Roy. Meteor. Soc.*, **114B**, 1321-1346.
- Déqué, M., C. Dreveton, A. Braun and D. Cariolle, 1994. The ARPEGE/IFS atmosphere model: a contribution to the French community climate modelling. *Climate Dyn.*, **10**, 249-266.
- Déqué, M. and Piedelievre, J.P., 1995. High-Resolution climate simulation over Europe. *Climate Dyn.*, **11**, 321-339.
- Lorant, V., and Royer, J.F., 2001. Sensitivity of equatorial convection to horizontal resolution in aquaplanet simulations with a variable-resolution GCM. *Mon. Wea. Rev.*, **129**, 2730-2745.

Energetics of African Easterly Waves using the Canadian Regional Climate Model (CRCM): A first approach.

Leticia Hernández Díaz and René Laprise

Département des Sciences de la Terre et de l'Atmosphère, UQAM, Montréal, Québec, Canada.

The Lorenz energy cycle of African Easterly Waves (AEWs) as simulated by the Canadian Regional Climate Model (CRCM), has been calculated.

The CRCM uses a semi-implicit, semi-Lagrangian numerical scheme to solve the fully elastic non-hydrostatic Euler equations (Laprise *et al.* 1997) and the subgrid-scale physical parameterization package of the second-generation Canadian Centre for Climate modelling and analysis atmospheric General Circulation Model (CCCma AGCM 2) (McFarlane *et al.*, 1992). A complete description of the numerical formulation of the model and the principal characteristics of the physical package can be found in Caya and Laprise (1999). In the present work, we use the version 3.5 of the CRCM in which moist convection is parameterized using the Kain and Fritsch (1990) scheme. The model is driven by National Centers for Environmental Prediction (NCEP) atmospheric re-analyses and the Sea Surface Temperatures (SST) are from the Atmospheric Model Intercomparison Project (AMIP II) data.

A first simulation (simulation # 1) over a 171 by 75 gridpoint domain with 100-km grid spacing in the horizontal and 10 Gal-Chen (GC) levels in the vertical, was made for the period from May to September 1995. The data generated by this simulation were used to drive a second run of the model (simulation # 2) at higher resolution over a 151 by 81 gridpoint domain with 50-km grid spacing and 19 GC levels, for August 1995 (Fig. 1).

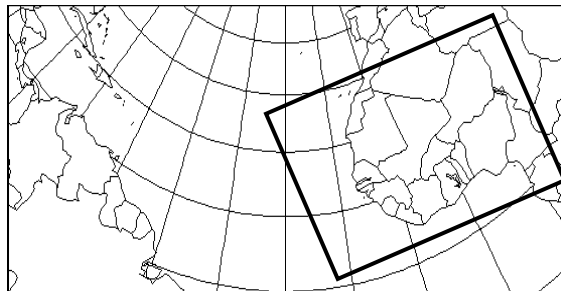


Figure 1. Computational domains. The largest domain corresponds to the simulation #1 with a 100-km grid increment and the smallest domain to the simulation #2 with a grid increment of 50 km.

Figure 2(a) displays a cross section between 5° and 25° N of the August 1995 mean zonal wind at 0° longitude (simulation #1). The main features of the wind structure in west Africa as simulated by the model are: a 600-700 hPa African easterly jet (AEJ) located between 15° and 20° N with a maximum wind speed of 8 - 10 m s⁻¹, an upper level tropical easterly jet (TEJ) at about 200 hPa equatorward of the AEJ, a low-level westerly flow to the south, and a westerly jet to the north. This is in agreement with the observational study of Reed *et al.* (1977) using Global Atlantic Tropical Experiment (GATE) data (23 August to 19 September 1974) averaged between 10°E and 31°W (Fig. 2b). A difference is that the simulated jet for 1995 is a little weaker than the analysed one in 1974 (10.0 m s⁻¹ vs 12.5 m s⁻¹, respectively).

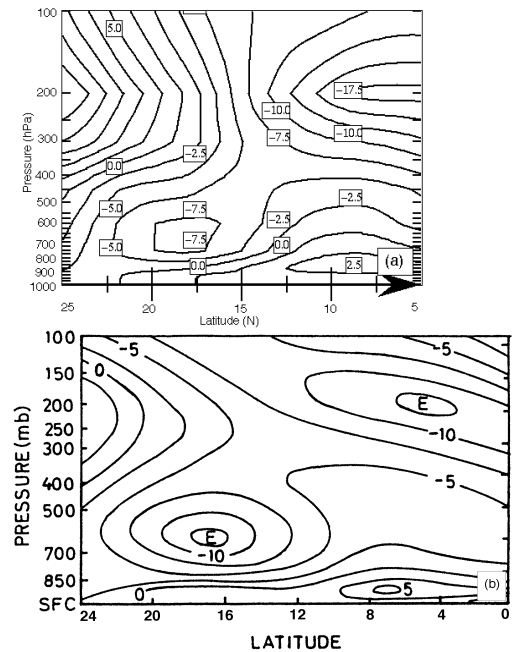


Figure 2. Mean zonal wind distribution over west Africa : (a) as simulated by the CRCM for August 1995 and (b) as obtained from GATE for the period 23 August to 19 September 1974 (after Reed *et al.*, 1977). The contour interval is 2.5 m s⁻¹.

AEWs can be identified in the fields of relative vorticity, winds, precipitation and sea level pressure. Figure 3 shows the CRCM-simulated relative vorticity at 700 hPa from August 11 to 14 (00Z) 1995, superimposed with the wind vectors at the same level.

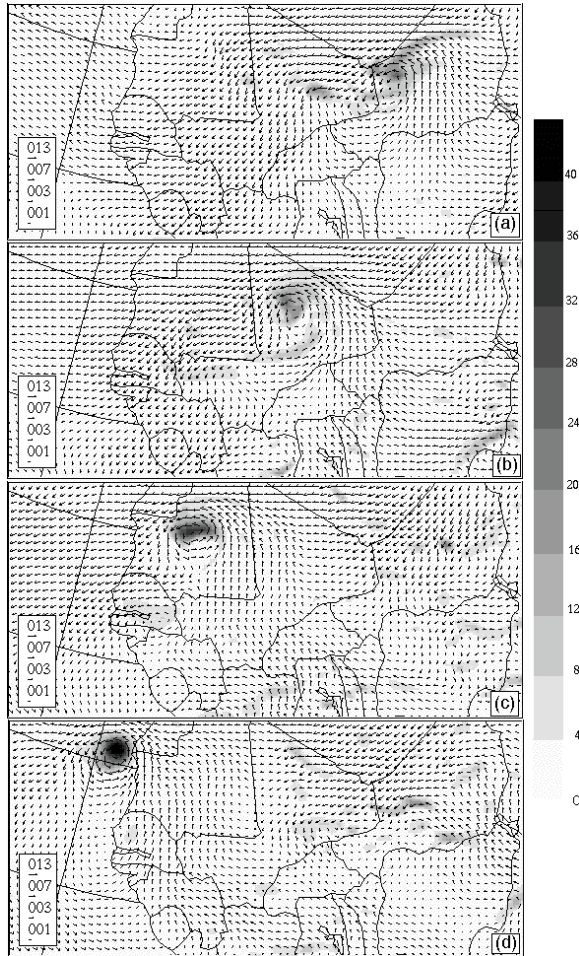


Figure 3. Relative vorticity in gray shade ($\times 10^{-5} \text{ s}^{-1}$) and winds vectors (m s^{-1}) at 700 hPa for the (a) 11th, (b) 12th, (c) 13th and (d) 14th August 1995 as simulated by the 50-km CRCM.

The Lorenz cycle is calculated using the equations for the time evolution of eddy energy in a limited-area domain as in Norquist *et al.* (1977), who followed the formalism developed by Muench (1965) for an open system, based on the seminal work of Lorenz (1955). The energy, conversion and generation terms are calculated over the entire CRCM computational domain (except the sponge zone) for the month of August 1995 (simulation #2). These are time-averaged to obtain the Lorenz cycle presented in Fig. 4. The vertical integrations have been made between 1000 and 350 hPa in order to concentrate on the interactions between the mid tropospheric jet (AEJ) and its effect over the AEWs. As it can be seen in Fig. 2, this allows to isolate the AEJ from the strong TEJ which could contaminate the computations.

On a monthly average basis, the eddy kinetic energy K_E is maintained by the barotropic energy conversion C_K and the baroclinic energy conversion C_E , the later being the more intense.

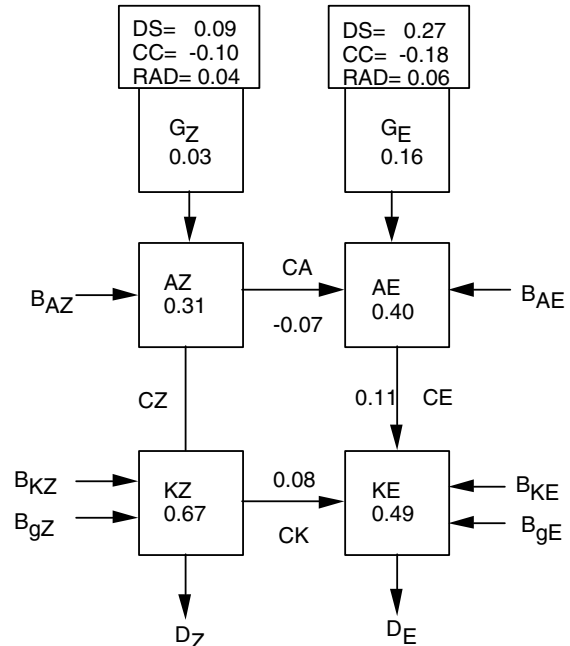


Figure 4. Lorenz diagram of the AEWs using the CRCM simulation for August 1995. Energies in J m^{-2} , conversions and generations in W m^{-2} .

The ratio of $K_E / (C_K + C_E)$ gives a doubling time of 2.6 days for the eddy kinetic energy which agrees well with the value of 2.9 days obtained by Norquist *et al.* (1977) for another year (23 August - 19 September, 1974). The generation ($G_E > 0$) of eddy available potential energy by diabatic processes is roughly of the same magnitude as the conversion terms. The largest contribution to G_E comes from the combined contribution of vertical diffusion and surface flux term, $G_E(\text{DS}) = 0.27 \text{ W m}^{-2}$. The combined contribution of the condensational heating and convective heat flux term, $G_E(\text{CC}) = -0.18 \text{ W m}^{-2}$, is negative in sign but has magnitude greater than the combined contribution of solar and terrestrial radiation term, $G_E(\text{RAD}) = 0.06 \text{ W m}^{-2}$ (which is the smaller). In our version of CRCM, the individual contributing components of Q_{DS} and Q_{CC} can not be obtained separately, so we can not say anything more about their relative strength. This is the reason why the contribution of the condensational heating, which is thought to be an important source of energy for the perturbations, can not be evaluated separately. The generation ($G_z > 0$) of zonal available potential energy is very weak in the domain, as expected for a tropical atmosphere (Newell *et al.*, 1972), but its sign is such as to maintain the meridional temperature gradient that is associated with the AEJ.

A « composite » of the energy and conversion terms for the three most intense perturbations of the month has been constructed and is shown in Figs. 5 and 6. The compositioning technique consisted in aligning the central time of the three most intense perturbations, and averaging them, taking five days on each side of the maximum. The remaining energy and conversion terms are similarly compositioned. It can be seen in Figs. 5 and 6 that the maxima in the conversion terms lead

that of the eddy kinetic energy, and that the most important conversion terms are those of the CK and CE. This conforms with the idea that the perturbations feed from the barotropic and baroclinic energy conversions (Burpee, 1972; Thorncroft, 1995). In the three composited systems, the baroclinic conversion seems to initiate the growth, followed 1 day later by barotropic conversion. The diabatic generation of eddy available potential energy, G_E , also contributes substantially in the period preceding the maximum intensity.

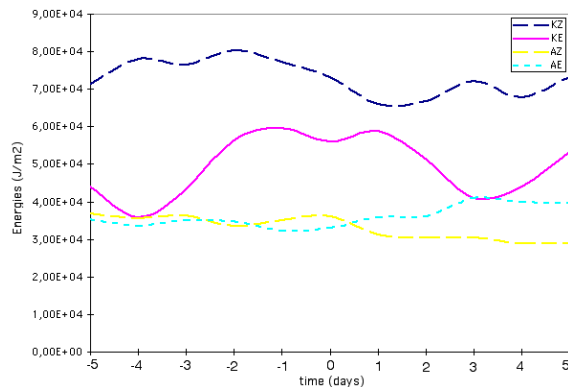


Figure 5. Composite of AZ, AE, KZ and KE (in $J m^{-2}$). Day 0 corresponds to the time of maximum AEW amplitude in the relative vorticity field.

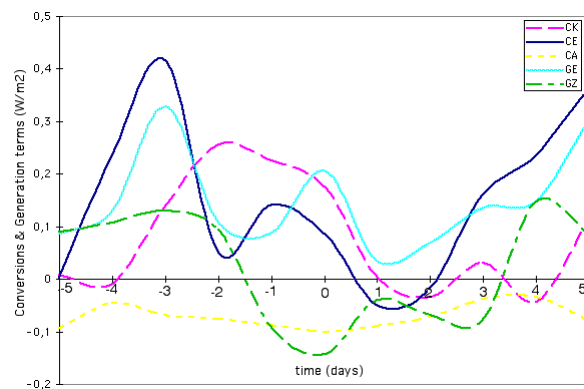


Figure 6. Composite of the conversion (CK, CE, CA) and generation (GE, and GZ) terms (in $W m^{-2}$).

References.

Burpee, R. W., 1972: The origin and structure of easterly waves in the lower troposphere of North Africa. *J. Atmos. Sci.*, **29**, 77 - 90.

Caya, D. and R. Laprise, 1999: A Semi-Implicit Semi-Lagrangian Regional Climate Model: The Canadian RCM. *Mon. Wea. Rev.*, **127**, 341 - 362.

Kain, J. S. and J. M. Fritsch, 1990: A One-dimensional Entraining/Detraining Plume Model and Its Application in Convective Parameterization. *J. Atmos. Sci.*, **47** (23), 2784 - 2802.

Laprise, R., D. Caya, G. Bergeron and M. Giguère, 1997: The formulation of André Robert MC2 (Mesoscale Compressible Community) model. The André J. Robert Memorial Volume (C. Lin, R. Laprise and H. Ritchie, Eds.), companion volume to *Atmos.-Ocean*, **35** (1), 195 - 220.

Lorenz, E. N., 1955: Available potential energy and the maintenance of the general circulation. *Tellus*, **7**, 157 - 167.

McFarlane, N. A., G. J. Boer, J.-P. Blanchet and M. Lazare, 1992: The Canadian Climate Centre Second-Generation General Circulation Model and Its Equilibrium Climate. *J. Climate*, **5**, 1013 - 1044.

Muench, H. S., 1965: On the Dynamics of the Wintertime Stratosphere Circulation. *J. Atmos. Sci.*, **22**, 349 - 360.

Newell, R. E., J. W. Kidson, D. G. Vincent and G. J. Boer, 1972: The General Circulation of the Tropical Atmosphere and Interactions with Extratropical Latitudes. The Massachusetts Institute of Technology, 370 pp.

Norquist, D. C., E. E. Recker and R. J. Reed, 1977: The energetics of African Wave Disturbances as Observed During Phase III of GATE. *Mon. Wea. Rev.*, **105**, 334 - 342.

Reed, R. J., D. C. Norquist and E. E. Recker, 1977: The structure and properties of African wave disturbances as observed during Phase III of GATE. *Mon. Wea. Rev.*, **105**, 317 - 333.

Thorncroft, C. D., 1995: An idealized study of African easterly waves. III: More realistic basis states. *Q. J. R. Meteorol. Soc.*, **121**, 1589 - 1614.

Address any correspondence to:
Leticia Hernandez Diaz (leticia@sca.uqam.ca) or
René Laprise (laprise.rene@uqam.ca).

Interaction between atmosphere and ocean-ice regional models over the Gulf of St-Lawrence area (Canada)

Manon Faucher¹, Daniel Caya¹, Francois Saucier² and René Laprise¹

1. UQÀM, C.P. 8888, Succ. "Centre-Ville", Montréal (Qc), H3C 3P8, Canada. faucher@sca.uqam.ca
2. Institut Maurice-Lamontagne, Mont-Joli (Qc), G5H 3Z4, Canada

1. Introduction

A numerical experiment using the Canadian Regional Climate Model developed at the "Université du Québec à Montréal" (CRCM, Caya and Laprise 1999) and the Gulf of St-Lawrence ocean model developed at the "Institut Maurice-Lamontagne" (GOM, Saucier *et al.* 2001) investigates the sensitivity of the models to each other with a series of simulations over Eastern Canada. The sensitivity of these models has already been investigated for short simulation by Gachon *et al.* (2001). However, we need to understand the interactions between the atmosphere, the ocean and the sea-ice over the Gulf of St. Lawrence (GSL) using these two models on a longer time scale. Furthermore, we wish to understand the role of these interactions in the present-day climate of Eastern Canada to develop a modelling strategy to perform regional climate change scenario for this area.

2. Experimental framework

A series of atmospheric and oceanic simulations are performed iteratively. The CRCM and GOM were run separately and alternatively over a fixed period of 5 months, using variables from the other model to supply the needed forcing fields. Each model computes its own surface budget of momentum, heat and freshwater at the interface between the atmosphere and the ocean-ice system from the exchanged variables. The study period is from November 1st, 1989 to March 31st, 1990, including a spinup of 1 month.

The computational domain of the CRCM is centered over the GSL (Fig. 1). It contains 99 by 99 grid points in the horizontal with a grid spacing of 30 km (true at 60°N) on a polar stereographic projection. There are 30 levels in the vertical between 131 m and 31 953 m. The timestep is 10 minutes. The lateral boundary conditions are obtained from the NCEP (National Center for Environmental Predictions) analyses. The computational domain of GOM extends from the Strait of Cabot to Montréal and at the head of the Saguenay Fjord. The horizontal resolution is 5 km on a rotated-Mercator projection. The ocean is layered in the vertical with a uniform resolution of 5 m down to 300 m depth and 10 m below 300 m.

A first simulation begins the iteration with the CRCM (CRCM1) taking observations from the AMIP II database (Atmospheric Models Intercomparison Project, Gates 1992) to provide the initial oceanic forcing fields. The AMIP data includes the sea-surface temperature (SST) and sea-ice fraction (SIF) with a spatial resolution of 1 degree. The atmospheric fields of CRCM1 (incident solar radiation at the surface, cloud cover, precipitation, 10-m wind, 2-m temperature and humidity) are archived every 6 hours and are used to prescribe the atmospheric state for a first oceanic simulation with GOM (GOM1) over the same 5-month period. The once-daily archived results of GOM1 (SST, SIF and sea-ice thickness) are used to repeat the atmospheric run (CRCM2); the AMIP data are used to supply the oceanic state outside the GSL. This second atmospheric simulation is used to repeat the oceanic simulation (GOM2) and so on. The process is iterated 3 times to study the evolution of the CRCM and GOM solutions when the atmospheric or oceanic fields are updated from the previous run.

3. Results

The experiments show that GOM can provide high-resolution oceanic forcing variables compared with the interpolated AMIP data. However, the CRCM is rather insensitive to differences in the oceanic fields during our study period. For example, as a result of a 50% decrease in the sea-ice cover in the GSL from the interpolated AMIP to the GOM1 data in December 1989, the difference in monthly mean temperature at 975 hPa (CRCM2 minus CRCM1) is at most 2.7°C locally along the West Coast of Newfoundland (Fig. 1a). Furthermore, the difference is restricted to the low level of the atmosphere and vanishes at 900 hPa. However, the warming of the air above the GSL is responsible for further reduction in the sea-ice and an increase in the ocean surface circulation from GOM1 to GOM2. On Fig. 1b, the monthly mean sea-ice extends over a large part of the GSL in GOM1, but it is restricted to the western half of the GSL in GOM2. The results have also shown that the sea-ice fraction is reduced by 10% to 15% and thinner in GOM2, compared with that in GOM1 (not shown). On Fig. 2, the monthly mean surface currents for December 1989 show relatively large differences from GOM1 to GOM2. In particular, the Gaspé current flows along the Gaspé Peninsula in GOM1 (Fig. 2a), while it is detached from the coast and extends further east in GOM2 (Fig. 2b). This experiment indicates that the position of the Gaspé current follows an area of slightly warmer, less stable atmospheric conditions and stronger winds, in relation with the sea-ice distribution. The warming trend has continued into the third iteration, but with reduced amplitude. The 975-hPa air temperature difference (CRCM3

minus CRCM2) is smaller, reaching 1.8°C south of Anticosti Island (not shown). On Fig. 1b, the sea-ice cover in GOM3 is further reduced, with the position of the edge approximately 30 km west of that in GOM2. Two additional iterations have been done for December 1989 to verify and confirm the convergence of the solutions for both, the CRCM and GOM. The results show that the differences in various fields become smaller as the number of iterations increases.

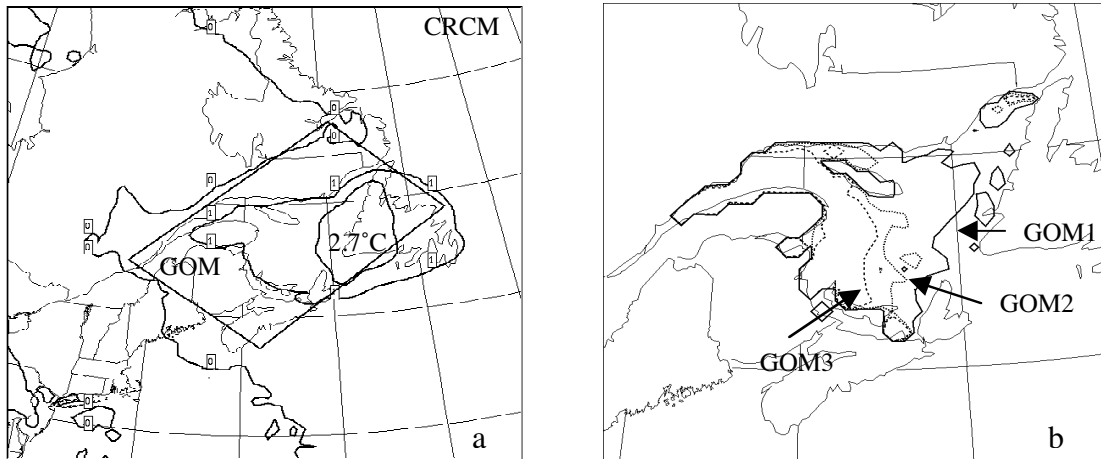


Figure 1. (a) Model domain of CRCM, including GOM's domain within the rectangle. Contours are the difference of monthly mean 975 hPa temperatures for December 1989 every 1°C (CRCM2 minus CRCM1). (b) Monthly mean sea-ice fraction (%) for December 1989 from GOM1 (solid line), GOM2 (dotted line) and GOM3 (dashed line).

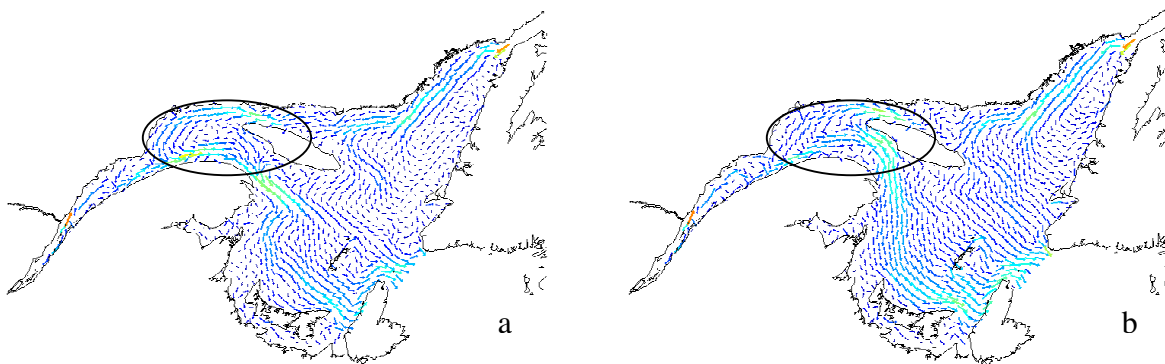


Figure 2. Monthly mean surface current (m s^{-1}) for December 1989 from (a) GOM1 and from (b) GOM2. The ellipses highlight the Gaspé Current.

4. Concluding remarks

The results of this experiment show that, on a monthly or longer time scale, the CRCM is not very sensitive to the oceanic fields from GOM, except locally in the Gulf area and near the surface. However, GOM is relatively sensitive to small differences in the atmospheric forcing from the CRCM. An important result is the convergence of the solutions, indicating that both models are reaching equilibrium with respect to each other. The sensitivity of the models to each other was investigated for a winter season. However, we need to continue the study over an annual cycle.

References

- (1) Caya, D. & R. Laprise, 1999: A semi-implicit semi-lagrangian regional climate model: The Canadian RCM. *Mon. Wea. Rev.*, 127, 341-362.
- (2) Gachon P., F.J. Saucier & R. Laprise, 2001: Atmosphere-ocean-ice interaction processes in the Gulf of St. Lawrence: numerical study with a coupled model. Scientific presentation. 6th Conference on Polar Meteorology and Oceanography and the 11th Conference on Interaction of the Sea and Atmosphere, AMS meeting, San Diego (California, USA), 14-18 May 2001.
- (3) Gates, W.L., 1992: AMIP: The Atmospheric Model Intercomparison Project, *Bull. Amer. Meteor. Soc.*, 73, 1962-1970.
- (4) Saucier, F.J., F.Roy, D.Gilbert, P.Pellerin & H. Ritchie, 2001: Modelling the formation and Circulation Processes of water masses and sea ice in the Gulf of St.Lawrence, Canada, *J.Geophys. Res.* Accepted.

Investigation of hydrology simulated by the Canadian Regional Climate Model over Québec and Labrador.

Anne Frigon¹, Michel Slivitzky² and Daniel Caya¹

¹UQÀM, Dept. Sciences de la Terre et de l'Atmosphère, frigon.anne@uqam.ca

²INRS-ETE (Institut national de recherche scientifique), Québec (Québec), Canada

We present here an investigation of the Canadian Regional Climate Model's (CRCM) surface hydrology over the vast Québec territory using a basin approach. The analysis is based on an additional year from the validation found in Frigon et al. (2002). In the experiment, the CRCM simulations were computed on a 100 X 100 point grid domain with a horizontal grid-point spacing of 30 km that covers mainly the Québec province and the Labrador territory. The model was configured with 18 vertical levels ranging from the surface to the model top at 29 km. The simulation starting on the 1st June 1992 and ending on the 31st May 1995 uses a 10-minute time step. The first three months, needed to spin-up the model and allowing the different fields to adjust to each other, were not retained for analysis. This version of the model (v3.5) was run with the Bechtold-Kain-Fritsch (Bechtold et al. 2001) mesoscale convective scheme along with a large-scale condensation process for stratiform precipitation formation. The other characteristics of the CRCM can be found in Caya and Laprise (1999). The CRCM was nested at its boundaries with atmospheric objective observational analyses from the National Center for Environmental Protection (NCEP), available every 12 hours with an initial horizontal grid-point spacing of 2.5° X 2.5° (approximately 275 km) and 12 vertical levels. The NCEP horizontal winds were blended over a nine-point nesting zone. Monthly climatological values of sea surface temperature (SST) and sea-ice cover were used for ocean grid points.

Amongst the 10 river basins that were studied, the Churchill Falls basin, covering an area of 69 300 km², is of particular interest owing to its enhanced precipitation network of 17 monthly surface stations. Fig. 1 shows that the CRCM precipitation agrees with the observations in winter but that the model produces too much precipitation from April to October. We are presently implementing a new stratiform precipitation scheme (Lohmann and Roeckner 1996) into the CRCM and preliminary results are promising; this should reduce some of the precipitation biases.

We also examined the CRCM's thermal regime at screen level. With more than one weather station in its vicinity, the Bell and Waswanipi basins (Western Québec, covering respectively 22 200 km² and 31 900 km²) were of particular interest. Fig. 2 shows that the CRCM monthly mean temperatures generally follow the observations in winter but remain too warm in summer. It is generally minimum temperature that is too warm and this behavior seems related to a too important cloud cover in the model; we are currently trying to verify this. Moreover, with its one layer surface scheme, the CRCM is generally too warm in fall and too cool in spring. This behavior can be explained, in fall, by the ground layer that must freeze throughout before cooling its surface below 0°C; the reverse situation happens in spring.

If the CRCM's temperature were not as warm in October and November (when the model starts to freeze the ground), the model would generate solid instead of liquid precipitation, reducing its runoff and contributing to a more important snow cover. We have examined the combined quantity of the CRCM's snow cover and runoff starting in October over the Churchill Falls basin. At the end of winter, we find that this combined quantity is close to the observed snow cover (from the 17 obs. stations) for the three winters simulated by the CRCM. Hence, if it were less warm in fall, the CRCM could produce a good snow cover. For hydrological purposes, it is essential to generate a good snow cover at the end of winter as it is the major source for the spring runoff, which represents about 50% of the annual volume in this area of the globe.

Globally, over the ten basins studied (covering a total area of 314 010 km²), we find that the CRCM is able to reproduce the observed runoff at the annual scale. The model's runoff resulting from the atmospheric water flux convergence over the domain is correct but the model overestimates precipitation and evaporation, because it recycles too much water, a known deficiency of the CRCM single-layer surface scheme. For example, in the 1993-1994 hydrologic year (from April till March), on the Churchill Falls basin, the CRCM overestimates annual runoff observations by only 68 mm (for an obs. value of 477 mm) while it overestimates total annual precipitation observations by 470 mm (for an obs. value of

848 mm) and total annual surface evaporation data (Willmott and Matsuura 2000) by 316 mm. However, the difference between the CRCM simulated annual runoff and the observations is quite variable from one basin to the other and from one year to the next. It is difficult to interpret these results with just a few years of simulation. On one hand, by using monthly climatological SSTs and sea-ice cover, the CRCM's ocean grid points have an annual cycle that repeats itself each year which influences the climate simulated in the basins of interest. On the other hand, because of regional model's internal variability (Giorgi and Bi 2000), we must not expect them to reproduce exactly each precipitation event passing over the basins. In that sense, regional models are not deterministic at a relatively small spatial scale, especially in summer because of the convective nature of precipitation. With more weather events passing over an area, the internal variability's effect decreases. Hence, to take into account the CRCM's internal variability, we plan to produce a 10 year CRCM simulation to evaluate the model's climate by comparing it to the observed climate.

The analysis of the CRCM's hydrology has allowed us to note its potential despite some weaknesses mainly attributed to the over simplification of surface processes parameterized by a single-layer surface scheme. We plan to generate a longer CRCM simulation nested not only with atmospheric observational analyses but also with sea surface temperature and sea-ice observations. This should produce a more realistic climate over Québec which, we know, is influenced by great water masses such as the Atlantic Ocean, the Labrador Sea and Hudson's Bay.

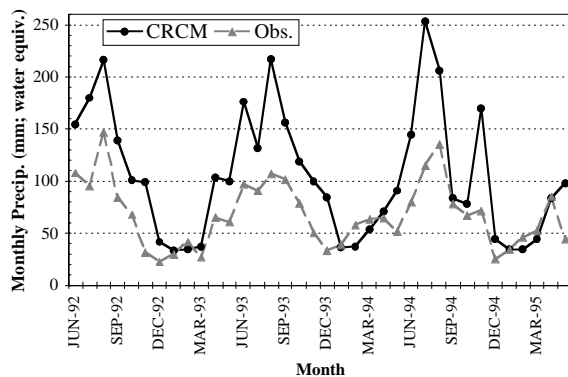


Fig. 1. Monthly precipitation over the Churchill Falls basin from the CRCM and the observations from June 1992 to May 1995.

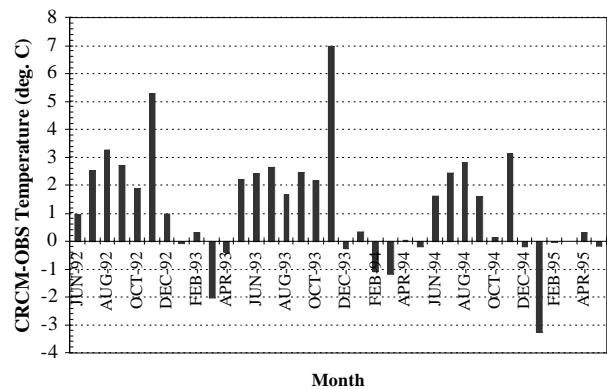


Fig. 2. Monthly mean screen temperature difference from June 1992 to May 1995 between the CRCM simulated value on the Bell/Waswanipi combined basins and the obs. from the Joutel, Chapais, Val d'Or surface weather stations.

References

- Bechtold, P., E. Bazile, F. Guichard, P. Mascart, and E. Richard, 2001: A Mass Flux Convection Scheme for Regional and Global Models. *Quart. J. Roy. Meteorol. Soc.*, **127**, 869-886.
- Caya, D., and R. Laprise, 1999: A Semi-Implicit Semi-Lagrangian Regional Climate Model: The Canadian RCM. *Mon. Wea. Rev.*, **127**, 341-362.
- Frigon, A., D. Caya, M. Slivitzky, and D. Tremblay, 2002: Investigation of the hydrologic cycle simulated by the Canadian Regional Climate Model over the Québec/Labrador territory. In: Beniston M. (ed), *Climatic Change: Implications for the Hydrological Cycle and for Water Management*. Advances in Global Change Research, 10. Kluwer Academic Publishers, Dordrecht and Boston.
- Giorgi, F. and X. Bi, 2000: A study of internal variability of a regional climate model. *J. Geophys. Res.*, **105**(D24), 29503-29521.
- Lohmann, U., and E. Roeckner, 1996: Design and performance of a new cloud microphysics scheme developed for the ECHAM general circulation model. *Clim. Dyn.*, **12**, 557-572.
- Willmott, C.J., and K. Matsuura, 2000: Terrestrial Water Budget Data Archive: Monthly Time Series (1950-1996). Version 1.0.1, released January 31, 2000. Data available through the University of Delaware, Center for Climatic Research Web site at <http://www.climate.geog.udel.edu/~climate>.

Regional Climate Model Inter-comparison Project for Asia

Congbin Fu *

*Project leader, START Regional Center for Temperate East Asia,
IAP/ Chinese Academy of Sciences, Beijing, CHINA 100029, E-mail: fcb@tea.ac.cn*

*Research team include:

Fu, C.B., Gutowski, W., Kato, H., Kim, J.W., Lee, D.K., McGregor, J., Sato, Y., Su, B., K., Wang, S.Y., Xiong, Z.

1, Introduction

To improve the simulation of regional climate change has been listed as one of the high priority areas in climatic change study, as it is the urgent requirement for usage in the impact assessment. Recent years there are an increasing number of research groups developing or using different versions of RCM to simulate the regional climate in Asia. Some studies have demonstrated that the RCM can reproduce the seasonal evolution of monsoon rain-belts over Asia that very often is not captured by the GCM. However it will be of great benefit for the further improvement of RCMs applications in Asia if more systematic analysis of the RCM performance and the intercomparison of various RCMs in simulating the regional climate in Asia and to describe RCM's distinctiveness in comparison with the GCMs are taken.

This paper introduces briefly a Regional Climate Model Inter-comparison Project (RMIP) for Asia under the joint support of Asia-Pacific Network for Global Change Research (APN), Global Change System for Analysis, Research and Training (START) and Chinese Academy of Sciences (CAS) and several projects of participating nations. The project is a joint effort of 10 research groups from Australia, China, Japan, S. Korea and United States, but also involve scientists from India, Italy, Mongolia, North Korea and Russia.

The designed tasks include three phases to be implemented in four years since 2000: phase one, 18 months run from April 1997 to September 1998 which includes a full annual cycle and two extreme cases to assess the model performance in reproducing the annual cycle of monsoon climate and capturing the extreme climate events; phase two, 10 years run from January 1989 to December 1998 to assess the statistical behavior of the models; and phase three, to project the climate scenarios of the 21st century by nesting the RCM with the GCM.

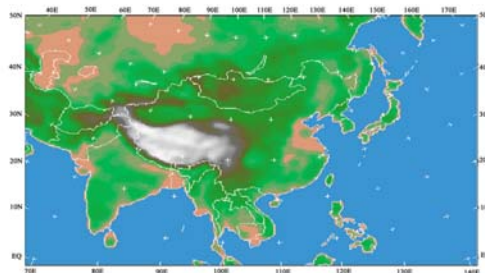


Fig.1. Simulation domain

Figure 1 presents the domain of model simulation, which includes most of Asia continent and part of western Pacific, Arabian Sea, Bay of Bengal and South China Sea, with the center at 35N/105E. It has the horizontal grid resolution of 60 km, with the grid numbers in longitude and latitude of 151x111. A relaxation lateral boundary treatment and, in some cases, a spectral nesting scheme are to nest with large scale forcing and 10 grids buffer zone is used. The domain for analysis is the inter part area with the buffer zones subtracted from each side of the integrated domain. It is divided into 12 sub-regions as shown in Figure 2. The models are driven by the large-scale fields either from observational data (e.g. NCEP analysis data) or GCM outputs at 6 hours interval. The land cover data set used in the simulation is the land cover classification derived from Global data sets for land-atmosphere

models, International Satellite land cover surface climatology project (ISLSCP), initiative 1,1987-1988,vol.1-5, at 1°x1° resolution (Meeson, B.W. et al, 1995), which then is interpolated into each grid point. The topography data with the resolution of 0.5X0.5 degree from National Center for Atmospheric Research (NCAR) is used for this study.

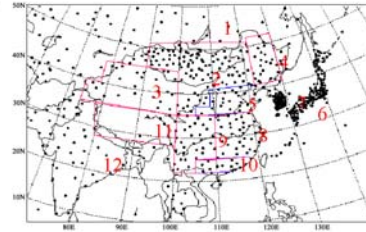


Fig.2. Distribution of stations and classification of sub-regions

The validation data for the model simulations against the observation are as following:

1) Station data There are totally 514 observation stations with daily records used for validation, including 193 from China, 155 from Japan, 72 from Korea, R.O., 6 from D.P.R.Korea, 73 from Mongolia and 15 from India. The data set is collected through regional collaboration. It is unique for being much more close to the reality as the observation than NCEP reanalysis data, although there are only few daily station data available over certain areas. The distribution of the stations is shown in Figure 2.

2) Grid data For the areas where there are only few station data to be used for validation, a number of grid data sets including global monthly precipitation data from Xie & Arkin for precipitation, NCEP reanalysis data for maximal/minimal temperature, Japan Meteorological Agency data for sea level pressure are utilized after interpolating into model resolution.

2, the results of phase one-the 18-month run

(1) Temperature

- I. All the models can reproduce the spatial patterns and the annual variation of mean, maximal and minimal temperature
- II. Nearly all models have the cold bias over most sub-regions, but the bias in the lower latitudes are smaller than those of higher latitudes;
- III. All the models have the largest bias in the arid/semi-arid region of northern domain.

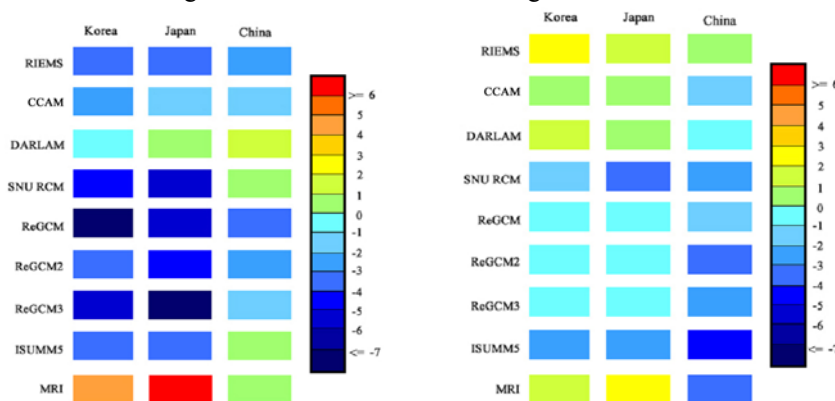


Fig.3. Seasonal averaged surface air temperature bias (a) left in winter 1997, (b) right in summer 1998

For more quantitative assessment, Figure 3 presents the bias of mean temperature simulation in China, Japan and Korea where more dense station data are available for validation. In winter (Figure 3a), there are overall cold bias in all models' simulation on-averaged of -4°C , except for MRI model of Japan which has warm bias over there regions with maximum of $5-6^{\circ}\text{C}$ over Korea and Japan. DARLAM model of Australia shows the best

performance in winter temperature simulation with the bias of $\pm 1^\circ\text{C}$. In summer (Figure 3b), most models also show cold bias over three regions in the range of -1 to -4°C , while RIEMS model of China shows warm bias in $1-3^\circ\text{C}$ ($< 1^\circ\text{C}$ over China, $< 2^\circ\text{C}$ over Japan and $< 3^\circ\text{C}$ over Korea). DARLAM and MRI show also warm bias over Japan and Korea in $1-3^\circ\text{C}$.

(2) Precipitation

- I. Nearly 50% of the models can reproduce the spatial pattern of seasonal total precipitation; the degree of agreement in winter is better than that of in summer;
- II. Nearly all the models reproduce the seasonal cycle in most sub-regions, except in, e.g. west arid/semi arid region;
- III. Models tend to overestimate the precipitation in higher latitude regions, e.g., in East arid/semi arid region, West arid/semi arid region, and North China;

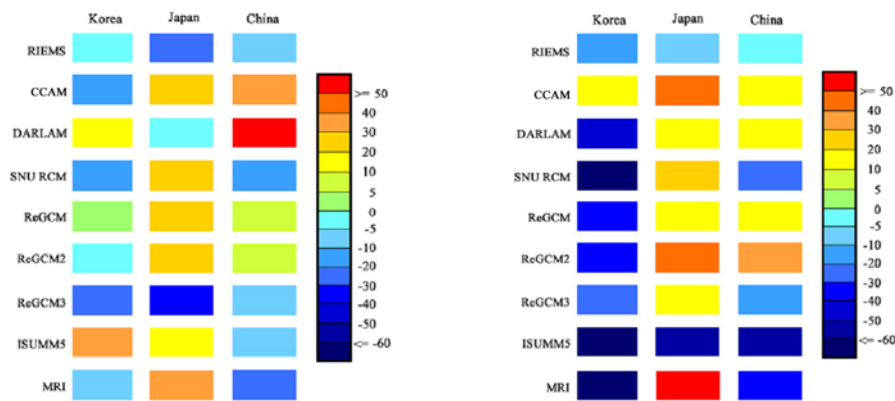


Fig.4. Seasonal total precipitation bias (%) (a) left in winter 1997 (b) right in summer 1998

Same as temperature, three areas of China, Japan and Korea are chosen for more quantitative assessment of the bias in precipitation simulations as shown in Figure 4. In winter, most models show bias in the range $< \pm 30\%$, while in summer most models show dry bias in Korea, but wet bias over Japan. There are mixed \pm bias from different model over China: CCM shows wet bias, while RIEMS and ISU/MM5 show dry bias.

In order to understand the possible reasons of bias in surface climate simulation, the atmospheric circulation both in lower and higher altitudes are analyzed further.

(3) Sea level pressure

- I. Most models reproduce the domain of Siberia High in winter, but the location and the intensity of the system center are in less agreement with the observation;
- II. Sub-tropical High in summer is captured by most models, but it extends further northwestwards than the observation. This supports the northern shift of simulated rain-belts in summer.

(4) Atmosphere circulation

- I. Nearly 70% of models can reproduce the location and intensity of both South Asia High and Westerlies over 200hpa properly;
- II. Most models capture the locations of Sub-tropical High and Low-Level Jet over 850hpa, but nearly 50% of models tend to overestimate the magnitude of Low-Level Jet;
- III. Nearly 70% models simulate successfully two S-N water vapor transport centers, but their intensities are not well simulated.

(5) Land-surface physics

- I. Simulated patterns of both sensible heat and latent heat are reasonable, e.g, the major center of sensible flux matches the location of Kuroshio warm current in winter, while it is over the heated land in summer;
- II. Most models' surface run-off patterns are in agreement with those of precipitation either in summer or in

winter

(6) Extreme events

- I. Nearly 50% of the models can reproduce the hot summer of 1997 over large part of Asia continent;
- II. There is overall northward shift of rain belts in summer in most of models and nearly 70% of models underestimate the intensity of heavy rain in Yangtze valley in June 1998, but the heavy rainfall center in second dekad of June is well capture by nearly 50% models;
- III. The models with better precipitation simulation show good performance to reproduce the upper/lower level jets. However, models with reasonable circulation simulation do not necessarily give the right simulation of precipitation.

Further analysis of the 18-months run is still going-on. In the meantime, the preparation for the 10-year simulation are taking place and phase 2 simulation and preliminary analysis on the statistical behaviors of all participating models will be accomplished in 2002-2003.

THE LINKAGE OF REGIONAL CLIMATE MODELS TO CROP MODELS

Deborah E. Hanley¹, Shrikant Jagtap², Timothy E. LaRow¹, James W. Jones², Steve Coker¹,
David Zierden¹, and James J. O'Brien¹

¹The Center for Ocean-Atmospheric Prediction Studies, FSU, Tallahassee, Florida

²University of Florida, Gainesville, Florida

1. INTRODUCTION

Agriculture is Florida's most weather-sensitive sector. There is a well-documented interest by growers and ranchers in Florida for advance information on the climate of the upcoming agricultural season. Seasonal forecasts offer the potential to modify outcomes and risks, and hence, impact decisions.

Future improvements in climate prediction science and forecast products are expected to come largely through larger ensemble datasets and improved dynamic climate models whose output can be used directly for agricultural applications (Phillips et al., 1998; Cane 2001; Druryan et al., 2001; Goddard et al., 2001). Therefore, even though their skill levels are still being investigated, it may be beneficial to couple agricultural models with the regional climate models for producing relevant information for use by agricultural decision makers.

The appropriate methodology for linking climate prediction and crop simulation models has been identified as a critical knowledge gap. The goal of this work was to examine these issues through a case study involving the integration of the Florida State University regional nested climate model (Coker and LaRow, 2000) with a maize model in the widely used DSSAT family of crop models. The growing seasons during 1998 and 1999 were chosen because they represent significantly different climate regimes: 1998 was an El Niño year and 1999 was a La Niña year. Descriptions of the climate models and crop models will be summarized in Sections 2 and 3. Preliminary results from this study will be discussed in Section 4.

2. NESTED REGIONAL SPECTRAL MODEL

The climate model used in this study is a regional spectral model embedded within a global coupled ocean-atmosphere spectral model. The regional model is a re-locatable spectral perturbation model that can be run at any horizontal resolution and uses base fields and sea surface temperatures derived from the coupled global model as boundary conditions. The vertical structure of the global model consists of 14 unevenly spaced vertical levels and it is coupled to the Max Planck global ocean model (HOPE). Details of these models and the model physics are available in Coker and LaRow (2000).

Two six-month experiments were conducted for the growing seasons (March-August) of 1998 and 1999. A ten-member ensemble was constructed for each year to assess uncertainty in initial conditions and variability of forecasts in space and time. Each ensemble member was six months (184 d) long with

atmospheric initial conditions chosen from consecutive start dates centered on 1 March, obtained from the European Centre for Medium-Range Weather Forecasts (ECMWF). The coupled model was initialized with a spun-up ocean state [see Coker and LaRow (2000) for more details]. The global model was run on a coarse grid spacing of ~200 km and the regional model on a fine scale resolution of ~20 km.

3. CROP MODEL

The CERES-Maize simulation model (Ritchie et al. 1998) was used to delineate effects of various forecasts on simulated maize yield. The CERES-Maize model is a dynamic process based crop model that simulates how corn plants respond to soil, weather, water stress, and management. Using site-specific input data, it calculates development, growth, and partitioning processes on a daily basis, starting at planting and ending when harvest maturity is predicted. As a result, the response of the corn plant to different soils, weather, and management conditions can be predicted.

4. DISCUSSION

In 1998, none of the forecasts (measured by either mean or most likely yield) predicted the 1998 yield of 7.2 Mg ha⁻¹ correctly (Figure 1). The yield simulated using 1998 weather was significantly lower than yields produced by all forecasts. The differences in maize yield forecasts arise because of the non-linearity of crop responses to weather. Expected yields from 30-yr of historic weather data ranged from 6.12 to 11.89 Mg ha⁻¹ with a mean of 9.90 Mg ha⁻¹ and standard error (s.e.) of 0.25 Mg ha⁻¹. The range of yields estimated in El Niño years was smaller and ranged from 9.10 to 11.84 with a mean of 10.31 and s.e. of 0.37 Mg ha⁻¹. The 1998 yield of 7.2 Mg ha⁻¹ was outside the range of yields expected using El Niño forecasts. Climatologically and using regional model forecasts, the probability of such a low yield was about once every 10 years or 10%. Prediction error (PE) (measured as the difference between the expected yield using a forecast and yield in 1998 using the same forecast specific management) varied from a low of +2.7 Mg ha⁻¹ using climatological forecast to a high of +3.80 Mg ha⁻¹ using regional model based forecasts.

The 1999 cropping season was a La Niña year with normal rainfall and resulted in a simulated yield considerably higher (13.94 Mg ha⁻¹) than yields predicted using 30-yr of climatological or 6-yr of La

Niña based forecasts (Table 1). The regional model-based forecast accurately predicted the observed 1999 yield (Figure 1). Predictions based on climatology, ENSO, and rainfall categories in 1998 and 1999 exhibited little skill, while the regional model forecast the 1999 yields with more accuracy.

5. CONCLUSIONS

We face many challenges as we seek to enhance the exciting prospect of bringing scientific seasonal climate forecasts to bear on agricultural systems. Presently, there is a capability to forecast synoptic weather (daily rainfall, temperatures and global solar radiation) specific to location/region by regional models nested within global models driven by the present state of the oceans. Results from this preliminary study indicate that the regional climate model exhibits some skill in the prediction of crop yields. More work needs to be done to evaluate the skill of the model and to determine if the model has similar skill during other seasons, different locations, or different crop types. Improvements to the model physics are currently underway and the newer version of the model will be tested in the near future. More details of these results are available in Jagtap et al. (2001).

6. ACKNOWLEDGEMENTS

The Center for Ocean–Atmospheric Predictions studies (COAPS) receives its base funding support from the Secretary of the Navy Grant to James J. O'Brien. This work was supported by NOAA and represents a cooperative effort between COAPS and the University of Florida. All climate models are run at COAPS and crop models are run at the University of Florida.

7. REFERENCES

- Cane, M. A., 2001: Understanding and predicting the world's climate system. *Impacts of El Niño and Climate Variability on Agriculture*. C. Rosenzweig, K. J. Boote, S. Hollinger, A. Iglesias, and J. Phillips, (Eds.), ASA Special Publication No. 63, American Society of Agronomy, Madison, Wis., USA, 1-20.
- Cocke, S., and T. E. LaRow, 2000: Seasonal predictions using a regional spectral model embedded within a coupled ocean–atmosphere model. *Mon. Wea. Rev.*, **128**, 689–708.
- Druyan, L. M., Fulakeza, M., Lonergan, P., and Saloum, M., 2001: A regional model study of synoptic features over West Africa. *Mon. Wea. Rev.*, **129**, 1564-1577.
- Goddard, L., S. J. Mason, S. E. Zebiak, C. F. Ropelewski, R. Basher, M. A. Cane, 2001: Current

Approaches to Seasonal to Interannual Climate Predictions. *Int. J. of Climatol.*, In press.

Jagtap, S. S., J. W. Jones, D. E. Hanley, J. J. O'Brien, and T. E. LaRow, 2001: Issues and challenges: Integrating regional spectral model climate forecasts with crop models. *In preparation*.

Phillips, J.G., M. A. Cane, C. Rosenzweig, 1998: ENSO, seasonal rainfall patterns, and simulated maize yield variability in Zimbabwe. *Agric. For. Meteorol.*, **90**, 39-50.

Ritchie, J. T., U. Singh, D. C. Godwin, and W. T. Bowen 1998: Cereal growth, development and yield. *Understanding Options for Agricultural Production*. G. Y. Tsuji, G. Hoogenboom, P. K. Thornton, (Eds.), Kluwer Academic Publisher, Dordrecht, The Netherlands, 79-98.

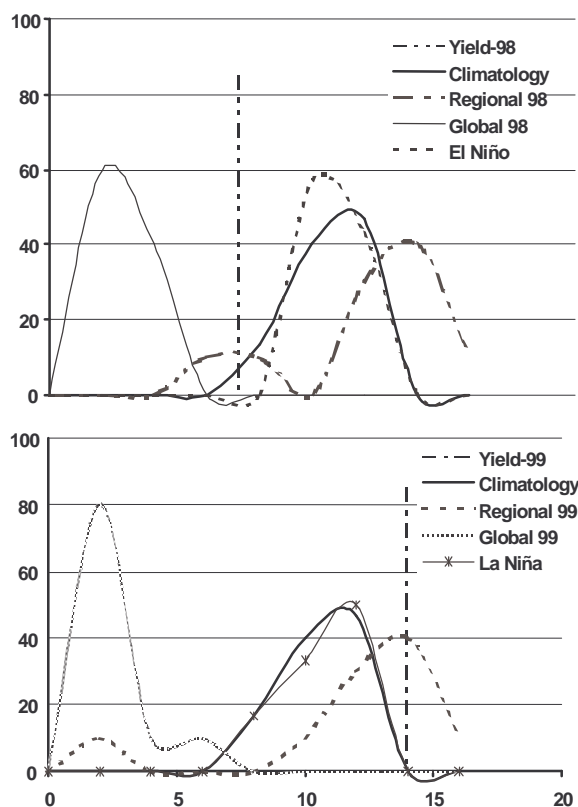


Figure 1. Relative frequency of maize yields forecast at Quincy, Florida, using different weather forecasting techniques and the current production practices for the (a) 1998 and (b) 1999 seasons. Yields were categorized into yield classes to create relative percentage values. More likely yields are indicated by higher percentages on the graphs. Figure reproduced from Jagtap et al. (2001b).

Chemistry and Climate Studies with the Met. Office Unified Model

R.S. Harwood, I.A. MacKenzie, and D.S. Stevenson
Institute for Meteorology, University of Edinburgh,
King's Buildings, Edinburgh, EH9 3JZ, UK. (iam@met.ed.ac.uk)

Overview

A variety of studies of the transport, chemistry and radiative effects of trace gases in the troposphere and middle atmosphere are being carried out with the UK Met. Office's Unified General Circulation Model (UM). The studies will contribute to understanding of the impact on climate and air quality of projected trends in anthropogenic emissions.

Inter-continental transport of ozone pollution

A global modelling study is being carried out to investigate how future changes in regional trace gas (NO_x , CO, VOC) emissions may affect tropospheric ozone. In the Intergovernmental Panel on Climate Change SRES A2 scenario used here, emissions from Southeast Asia are projected to grow much faster than the global average, whereas regions with strict controls (e.g., Europe), or faltering economies (e.g., Russia) show modest growth, or even decline. Simulations with fixed meteorology were performed for 1990 and 2030 emissions, along with additional 2030 runs with regional (Europe, North America, Southeast Asia) emissions reverting to 1990 levels. Increases in Asian emissions (see Figure 1) generate extra ozone in the upper troposphere over Asia and downwind, extending over the Pacific and North America. Subsequent downwards transport and mixing allows Asian emissions to influence ozone throughout the troposphere in northern middle latitudes. The most widespread effects are seen in late spring, a trade-off between the longer ozone lifetimes during winter and the higher ozone production efficiency during summer. Lesser impacts are seen from the more northerly European and North American emissions, partly explained by the smaller magnitude increases, but also due to less convective lofting of emissions to the upper troposphere. Clearly the location of ozone precursor emissions has a major influence on their ozone production efficiency.

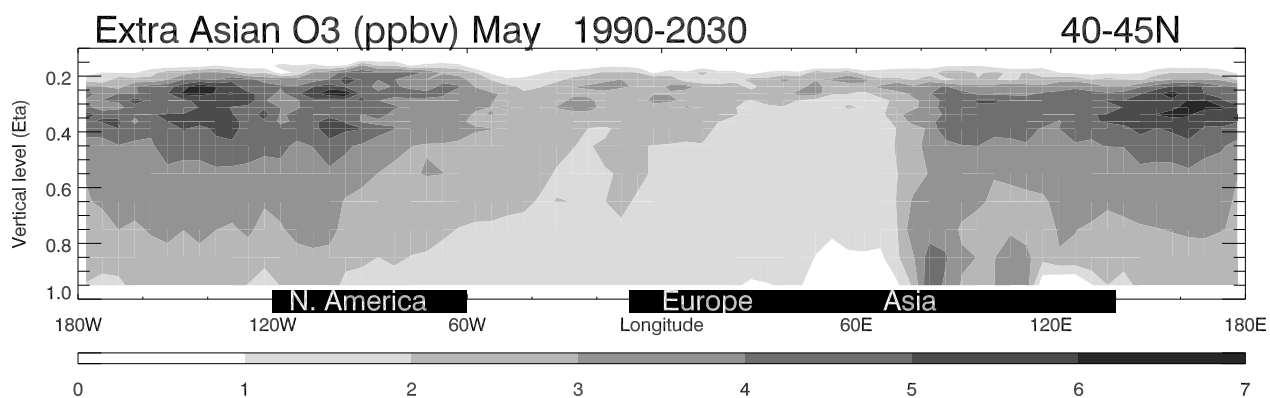


Figure 1: Simulated increase in tropospheric ozone between 1990 and 2030 due to anthropogenic trace gas emissions from Asia.

Impact of methane-derived water vapour on future middle-atmospheric climate

The UM with parameterized and interactive CH₄/H₂O/H₂ and O₃ chemistry is being used to examine the response of the middle atmosphere to an increase in its humidity caused by a possible future increase in CH₄. The chemical parameterization allows the middle-atmospheric H₂O change to evolve naturally from an imposed change in tropospheric CH₄. First, a control simulation of the present-day atmosphere is compared with a simulation of the year 2060 using postulated (IPCC SRES B2) concentrations of all the important long-lived, radiatively-active gases. Then, the particular contribution of the CH₄, and hence H₂O, change to the observed difference is isolated by comparing simulations of 2060 including and excluding the projected CH₄ change. The CH₄ and H₂O profiles from the different simulations are shown in Figure 2.

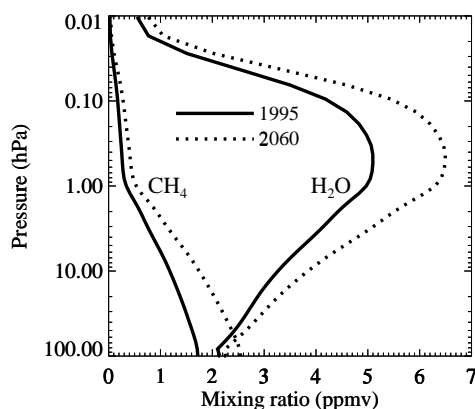


Figure 2: Annual, tropical mean profiles of CH₄ and H₂O from the 1995 and 2060 simulations.

Figure 3a shows the annual-mean temperature difference between 2060 and 1995 due to the combined influence of the change in all the radiatively-active gases. There is a general cooling of the 2060 middle atmosphere which peaks at around 5 K throughout the upper stratosphere and mesosphere. This nett cooling is due mainly to the increased CO₂ in 2060; the contribution of the increased H₂O to the temperature difference is indicated by Figure 3b. Over most of the middle atmosphere, the H₂O is responsible for a cooling of between 0.4 and 0.6 K or around 10% of the total temperature change between 1995 and 2060.

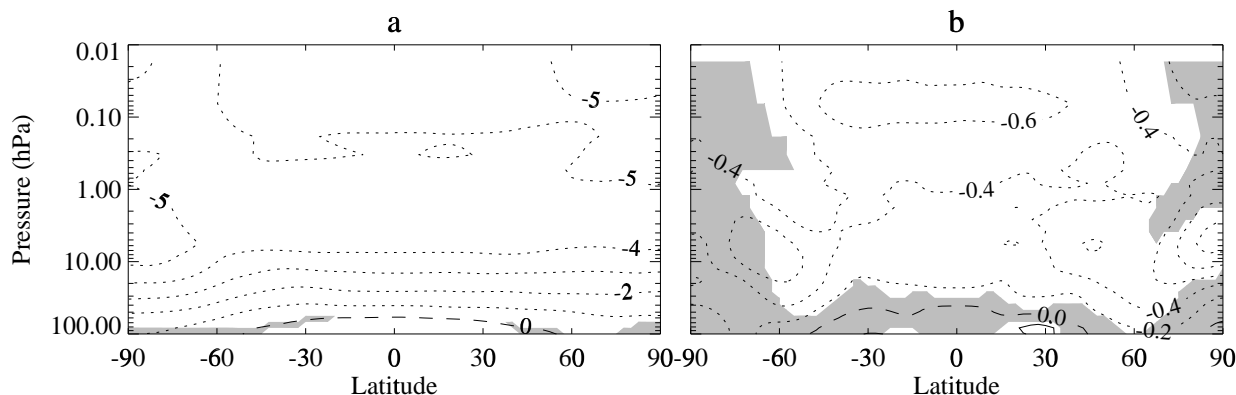


Figure 3: (a) Annual, zonal-mean temperature change (K) between 1995 and 2060 when all radiatively-active gases are adjusted in line with IPCC scenario SRES B2; (b) Individual contribution of the CH₄/H₂O adjustment to the total difference seen in (a). The shading indicates where the temperature difference is not statistically significant.

Analysis of water cycle changes in Siberian rivers basins in XX and XXI centuries from model simulations

Vyacheslav Ch. Khon
A.M.Obukhov Institute of Atmospheric Physics RAS
3 Pyzhevsky, 109017 Moscow, Russia
khon@omega.ifaran.ru

In this study, water cycle changes in the Siberian rivers basins, including rivers runoff, from transient runs of coupled general circulation models (CGCM) ECHAM4/OPYC3 with flux adjustment (Oberhuber 1993; Roeckner et al. 1996), HadCM3 without flux adjustment (Collins et al. 2001) and IAP RAS climate model (CM) of intermediate complexity (Petoukhov et al. 1998; Handorf et al. 1999; Mokhov et al. 2000) for the period 1860-2100 are analyzed (Mokhov and Khon 2000; Mokhov and Khon 2001b). Greenhouse gases changes in the atmosphere in these numerical experiments were taken from observations for the 1860-1990 and according to the IS92a scenario (Houghton et al. 1992) for the 1991-2100 period. For IAP RAS CM simulations with change only CO₂ content in the atmosphere are analyzed.

The river runoff Q was characterized by a difference between precipitation P and evaporation E on river watersheds. Model simulations were compared with observations for the Ob (1930-1994), Yenisei (1936-1995) and Lena (1935-1994) rivers runoff Q (e.g., Duemenil et al. 2000). In addition, different climatological data for precipitation and evaporation in rivers basins and runoff were used (e.g., Korzun et al. 1974; Vuglinsky 1998).

Table 1 presents mean values and standard deviations, SD, (in brackets) of the Ob (1930-1994), Yenisei (1936-1995) and Lena (1935-1994) rivers runoff from model simulations in comparison with observations for the same period and with different climatological estimates. There is a general agreement between model simulations and observations for the runoff mean values of Ob, Yenisei and Lena rivers, except for Lena river in IAP RAS CM with a significant runoff underestimation. General underestimation of the Lena river runoff in models is related with a general model overestimation of evaporation in the basin.

In general, model results exhibit an increase of mean values and variances of regional precipitation in the Ob, Yenisei and Lena rivers watersheds and rivers runoff to the Arctic Ocean in the XXI century relative to XX century (Mokhov and Khon, 2000). The general increase of the Siberian rivers runoff under the global warming in XXI century is connected with an increase of precipitation, especially in the Lena river basin. Model simulations display significant increase of precipitation in XXI century to the north from 50N (especially in winter). Alongside with such a general tendency a remarkable interdecadal variations of regional water cycle characteristics have been noted from model simulations. For instance, ECHAM4/OPYC3 and HadCM3 exhibit some decrease of the Ob and Yenisei rivers runoff in the first half of the XXI century.

The increase of the Lena and Yenisei rivers runoff from CGCM simulations steady exceed the level of standard deviations from observations at the NH warming larger than 1÷1.7K and 2.5÷3K, respectively (Mokhov and Khon, 2001b). The corresponding "critical" level for the Ob river runoff is reached only at the end of XXI century for ECHAM4/OPYC3. The corresponding changes with a 30-year moving average from HadCM3 simulations at the end of XXI century are remarkably less than the SD level from observations.

Analysis of connection of the Siberian rivers runoff with characteristics of atmospheric circulation in the Northern Hemisphere from observations and simulations was also carried out, in particular, with indices of the North-Atlantic Oscillation (NAO) and Arctic Oscillation (AO), characteristics of the atmospheric centres of action, including Siberian High (Mokhov and Khon, 2001b). It was found, for instance, statistically significant relationship (at 95 % level) of the Yenisei river runoff with the AO index, obtained from the NCEP/NCAR reanalysis data for the 1958-1995 period. The positive statistically significant correlation between the annual-mean Lena (Yenisei) river runoff and the winter (December - March) NAO index at 99% (95%) level was also revealed from observations. The annual-mean Yenisei river runoff and intensity of the winter Siberian High show negative correlation from observations for the period 1936-1995. The positive statistically significant correlation of the runoff of Lena and Yenisei with the NAO index is also shown for modelling results, in particular for ECHAM4/OPYC3 simulations.

This work was partly supported by the Russian Foundation for Basic Research.

References

- Collins, M., S.F.B. Tett, and C. Cooper, 2001: The internal climate variability of HadCM3, a version of the Hadley Centre coupled model without flux adjustments. *Clim. Dyn.*, 17, 61-81.
- Duemenil Gates, L., S. Hagemann, and C. Golz Observed historical discharge data from major rivers for climate model validation. *Max-Planck-Institut fuer Meteorologie, Rep.* No.307, 93 pp.

Handorf, D., V.K. Petoukhov, K. Dethloff, A.V. Eliseev, A. Weisheimer, and I.I. Mokhov, 1999: Decadal climate variability in a coupled atmosphere-ocean climate model of moderate complexity. *J. Geophys. Res.*, 104, 27253-27275.

Houghton, J.T., B.A. Callander, and S.K. Varney (eds), 1992: *Climate Change: The Supplementary Report to the IPCC Scientific Assessment. Intergovernmental Panel on Climate Change*. Cambridge University Press, 198 pp.

Korzun, V.I., et al. (eds.), 1974: *World Water Balance and Water Resources of the Earth*, Gidrometeoizdat, 638 pp.

Mokhov, I.I., A.V. Eliseev, D. Handorf, V.K. Petoukhov, K. Dethloff, A. Weisheimer, and D.V. Khvorostianov, 2000: North-Atlantic Oscillation: Diagnostics and modelling of decadal variability and its long-term evolution. *Izvestiya, Atmos. Oceanic Phys.*, **36**, 605-616.

Mokhov, I.I. and V.Ch. Khon, 2000: Diagnostics and modelling of hydrological cycle changes of the Siberian rivers basins in XX and XXI centuries. In: *Ecology of Floodplains of the Siberian Rivers and the Arctic*, 8-16. (in Russian)

Mokhov, I.I. and V.Ch. Khon, 2001a: Projections of future changes of hydrological cycle in the Caspian Sea basin. *Research Activities in Atmospheric and Oceanic Modelling. H.Ritchie (ed.)*. WMO/TD-No.1064. 9.20-9.21.

Mokhov I.I. and V.Ch. Khon, 2001b: Water cycle in basins of Siberian rivers: changes in XIX-XXI centuries from model simulations // *Proc. Fifth Intern. Study Conf. on GEWEX in Asia and GAME*. Nagoya. V.2. No.31(2). P.328-333.

Oberhuber, J.M., 1993: The OPYC Ocean General Circulation Model. *Max-Planck-Institut fuer Meteorologie, Rep.7*, 130 pp.

Petoukhov, V.K., I.I. Mokhov, A.V. Eliseev, and V.A. Semenov, 1998: *The IAP RAS Global Climate Model*. Dialogue-MSU, 110 pp.

Roeckner, E., K. Arpe, L. Bengtsson, M. Christoph, M. Claussen, L. Duemenil, M. Esch, M. Giorgetta, U. Schlese, and U. Schulzweida, 1996: The atmospheric general circulation model ECHAM4: Model description and simulation of present-day climate. *Max-Planck-Institut fuer Meteorologie, Rep.218*, 90 pp.

Vuglinsky, V.S., 1998: River water inflow to the Arctic Ocean - conditions of formation, time variability and forecasts. *Proc. of the ACSYS Conf. on Polar Processes and Global Climate*. WCRP-106. WMO/TD-No.908, 277-278.

Table 1.

P-E, mm/yr	Ob	Yenisei	Lena
ECHAM4/ OPYC3	146 (±31)	217 (±25)	166 (±27)
HadCM3	151 (±30)	237 (±36)	181 (±37)
IAP RAS CM	146 (±41)	256 (±61)	76 (±25)
Runoff, Q Observations	134 (±21)	233 (±18)	216 (±26)
P-E Climatologies	130÷135	237÷244	190÷214

Modeling the Variations of the North Atlantic Oscillation under Anthropogenic Scenarios

D.V. Khvorostyanov

Moscow State University,
Institute of Atmospheric Physics, Russian Academy of Sciences
e-mail: dimok@omega.ifaran.ru

The North Atlantic Oscillation is considered to be the dominant signal of Northern hemisphere wintertime decadal variability and to have a strong impact on the European winter climate.

This paper presents results of the IAP RAS climate model experiments under two anthropogenic CO₂ scenarios. The IAP RAS climate model is described in detail in Petoukhov et al. [1998]. It is an intermediate complexity model that employs splitting of physical processes into synoptic (with timescales of a few days) and larger-scale components. The latter are described by the model prognostic equations, while the former are parameterized. The model has 6x4.5° resolution, eight atmospheric, three oceanic, and two soil layers.

The first CO₂ increase scenario (IPCC IS92a, hereafter I) implies permanent concentration growth, and the second (II) refers to the constant CO₂ level after 1990 (Mokhov and Khon [2001]). Figure 1 shows the variations of the winter NAO index during 1860–2040 from the IAP RAS model for both scenarios and from the ECHAM4/OPYC3 model's greenhouse experiment (Roeckner et al. [1996]). The indices are smoothed by the running mean filter with the 30-year window length and normalized by the standard deviations (STDs) taken over 1861–1960. The mean value and STD are shown for the ECHAM4/OPYC3 model's control run by horizontal solid and dashed lines, respectively. As the figure indicates, the NAO index (both from IAP RAS scenario I and ECHAM4/OPYC3 models) continues to grow in the 20th century. The observed interannual NAO index dispersion is fairly reproduced by the IAP model: the observed STD for 1860–1997 equals 1.1, and the model yields 1.2 for both scenarios. For the ECHAM4/OPYC3 model the STDs equal 1.8 and 1.9 for the control and greenhouse experiment, respectively.

Amplitude and period of the NAO determine the strength and occurrence of its impact. The knowledge of how they change in time and how they are correlated could be useful in expecting their future changes. Using the method described in Mokhov and Eliseev [1997], time variations of NAO amplitude and period were calculated. Their relationship was estimated through the linear regression of the period (P) on the amplitude (A).

The linear regression of P on A is positive in the four cases considered: greenhouse and fixed runs of the IAP RAS model, control and greenhouse runs of the ECHAM4/OPYC3 model. This agrees with observed and reconstructed NAO index analysis (Mokhov et al. [2000b]). For the IAP RAS model forced by the IS92a (I) scenario, the regression is significant at $\geq 95\%$ level. The regression coefficient $b = 3.6 \pm 1.6$ mo, the correlation coefficient $r = 0.50$ at 15 degrees of freedom (DOF). With the scenario II, this A – P relationship turns to be significant only at the STD level: $b = 3.5 \pm 2.4$ mo, $r = 0.35$ at 16 DOF. For the ECHAM4/OPYC3 model, the control integration yields more significant positive regression of P on A than the greenhouse one. However, when considering only the variations with sufficiently high amplitudes (greater than a certain minimum value), the greenhouse forcing experiment gives much more significant result. For the amplitudes greater than 0.3 K, greenhouse run yields the A – P regression significant at $\geq 99\%$ level, while the control experiment gives only 90%–level significance.

These results allow one to conclude (see also Mokhov et al. [2000a]) that: 1) the amplitude and the period of decadal NAO variations change coherently in time, i.e., the amplitude rises are accompanied on average by period lengthening, and vice versa; 2) this positive amplitude–period correlation tends to amplify under the greenhouse forcing, at least for sufficiently strong amplitudes.

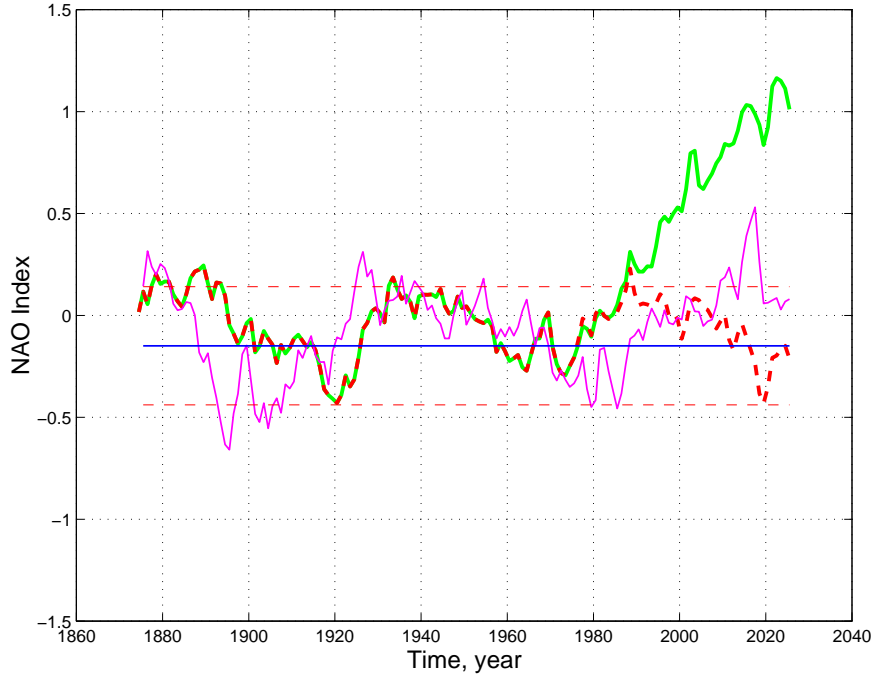


Figure 1: NAO index filtered by running means at the window $I_0=30$ yr. Thick lines, solid and dashed, show the IAP RAS model experiments, scenario I and II, respectively; thin lines refer to the ECHAM4/OPYC3 model: the curve denotes the greenhouse forcing run, and horizontal lines show the mean and the STD in the control experiment

This work was partly supported by the Russian Foundation for Basic Research.

References

- I.I. Mokhov, K. Dethloff, A.V. Eliseev, D. Handorf, V.Ch. Khon, D.V. Khvorostyanov, and A. Weisheimer. Quasidecadal variations of North Atlantic and Arctic Oscillations from long-term integrations of climate model of intermediate complexity and observations. In *Chapman Conf. "The North Atlantic Oscillation". Abstracts*, Ourense, 2000a. University of Vigo.
- I.I. Mokhov and A.V. Eliseev. Tropospheric and stratospheric temperature annual cycle: Tendencies of change. *Izvestiya, Atmos. Ocean. Phys.*, 33(4):415–426, 1997.
- I.I. Mokhov, A.V. Eliseev, D. Handorf, V.K. Petoukhov, K. Dethloff, A. Weisheimer, and D.V. Khvorostyanov. North Atlantic Oscillation: diagnosis and modeling of decadal variability and its long-term evolution. *Izvestiya, Atmos. Ocean. Phys.*, 36(5):605–616, 2000b.
- I.I. Mokhov and V.Ch. Khon. Projections of future changes of hydrological cycle in the caspian sea basin. In H. Ritchie, editor, *Research Activities in Atmospheric and Oceanic Modelling*, pages 9.20–9.21. World Meteorological Organization, WMO/TD No. 1064, 2001.
- V.K. Petoukhov, I.I. Mokhov, A.V. Eliseev, and V.A. Semenov. *The IAP RAS global climate model*. Dialogue–MSU, Moscow, 1998.
- E. Roeckner, K. Arpe, L. Bengtsson, M. Christoph, M. Claussen, L. Dümenil, M. Esch, M. Giorgetta, U. Schlese, and U. Schulzweida. The atmospheric general circulation model ECHAM-4: Model description and simulation of present-day climate. Technical Report 218, Max-Planck-Institut für Meteorologie, Hamburg, 1996.

Effect of mountain uplift on warm pool: a study with the new MRI coupled GCM

Akio Kitoh¹, Manabe Abe² and Tetsuzo Yasunari³

¹ Meteorological Research Institute, Tsukuba, Japan

kitoh@mri-jma.go.jp

² Graduate School of Geoscience, University of Tsukuba, Tsukuba, Japan

abe@luft.geo.tsukuba.ac.jp

³ Institute of Geoscience, University of Tsukuba, Tsukuba, Japan

yasunari@atm.geo.tsukuba.ac.jp

Large-scale mountains such as the Tibetan plateau, Rocky mountains and Andes mountains, play essential roles to form the present climate. Therefore those uplift was a major event in the natural history of the earth. For example, the uplift of the Tibetan plateau has led to the evolution and the variety of monsoon climate system in Asian region (e.g. Kutzbach et al. 1993). A number of geological evidence for climate changes due to the uplift has been found both over land and the ocean. However, as the climate change is forced not only the mountain uplift but also other forcing such as astronomical forcing, variation of CO₂ level and ice sheet extent in the past, it is difficult to separate the effect of the past mountain uplift. Therefore, experimental studies with an atmosphere and ocean coupled general circulation model (GCM) is needed to understand global influence, including the ocean, of the uplift.

In this study, the newly developed MRI coupled GCM (MRI-CGCM2, Yukimoto et al. 2001) is used. We integrated the control run with a realistic land-sea distribution and orography (M-run) and the anomaly run without a flat surface everywhere by keeping the same land-sea distribution (NM-run). Figure 1 shows the difference in annual mean precipitation between M-run and NM-run. The precipitation increases in the region between the eastern Indian Ocean and the western Pacific Ocean and in Asian region by mountain uplift, while precipitation decreases in the western Indian Ocean and the central Pacific Ocean. Particularly, a zonal contrast of precipitation in NM-run is reversed to that in M-run in the tropical Indian Ocean. Figure 2 shows the difference in annual mean sea surface temperature (SST). Over the tropical region in NM-run, the local SST maximum above 28°C is centered around the date line, while SST below 25°C is found in the eastern Indian Ocean, the eastern Pacific Ocean, and the eastern Atlantic Ocean. However, in M-run, SST above 28°C extends in the western Pacific Ocean as observed, which is in contrast with that in NM-run.

Furthermore, in the equatorial Indian Ocean, the SST gradient is reversed between the two runs. Thus, the formation of the western Pacific warm pool is controlled by mountain uplift through changes in monsoon circulation in our experiment. In addition to this study, we continue to investigate the influence of different altitude of mountains on the global climate.

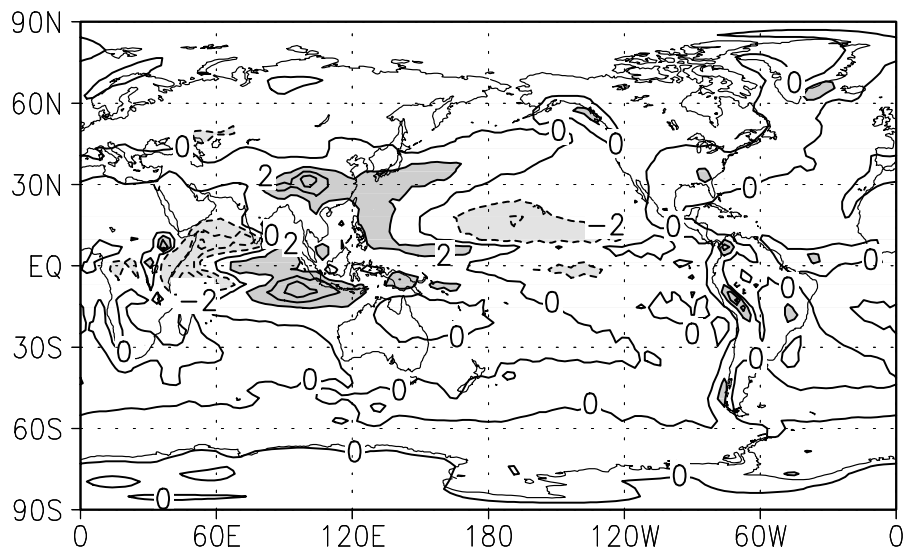


Figure 1: Annual mean precipitation difference between M-run and NM-run. The contour interval is 2 mm/day.

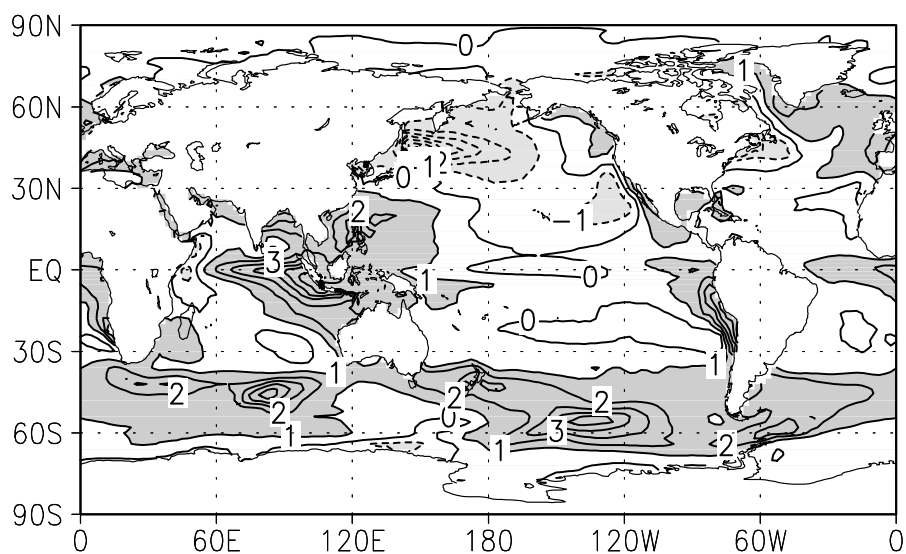


Figure 2: Annual mean SST difference between M-run and NM-run. The contour interval is 1°C.

Multi-Convection as a Multi-Model Proxy for Climate Studies
By Timothy E. LaRow and Steven Cocke
Florida State University
larow@coaps.fsu.edu

A different method of generating multi-model ensembles for climate integrations is developed. Instead of using multi-models, as currently being done by some of the major operational centers, we will use a single model, the FSU coupled model (LaRow and Krishnamurti 1998, Cocke and LaRow 2000), with six different state-of-the-art deep convective parameterizations. The six convection schemes are: Emanuel and Zivkovic-Rothman (1998), Zhang and McFarlane (1995), Krishnamurti et al (1983), Pan and Wu (1994), Moorthi and Suarez (1992) and Hogan and Rosmond (1991).

Experimental Details

Six model formulations are integrated for a 12 year (1986-1997) period. The integrations commence on 1 November of the respective year and continue for 210 days. The initial conditions for the atmospheric model are taken from 12UTC ECMWF analysis. The ocean initial conditions are taken from a continuous initialization procedure (LaRow and Krishnamurti 1998). This set of experiments is called MM (multi-model). A control integration was conducted for the same 12 years using the Pan and Wu convection scheme. This is the standard configuration used in the FSU coupled model. For each year, a five member ensemble was developed by varying the initial start date of the atmospheric model using consecutive start dates centered on 1 November. This set of experiments is called MA (multi-analysis). Weekly and monthly mean fields and anomalies are derived for both the MM and MA and are defined with respect to the individual model's climatology.

Results

The Relative Operating Characteristic (ROC) is used to quantify the skill of the forecast. The ROC is a probabilistic measure of the skill and the ROC curve is a plot of the hit rate vs. false alarm rate for the ensemble. The measure of skill is determined by the area under the ROC curve (see Palmer et al 2000). A perfect deterministic forecast will have an area equal to one while a forecast exhibiting no skill will have a value less than 0.5. The area under the SST ROC curves (A_{ROC}) for threats of 0.0° , 0.5° and 1.0° K in the Niño-4, Niño-3 and Niño-3.4 for all DJF ($n=36$) from the MM and MA are shown in Table 1. Reynolds and Smith (1994) weekly SST was used for the observations. The larger values are in **bold**. Both the MM and MA show skill greater than 0.5; however, the MM A_{ROC} score is consistently larger compared to the MA's score. The Niño-3 region shows the highest average skill for both the multi-model and multi-analysis. The Niño-4 region shows the least amount of skill for the MM and MA. The diminished skill in the Niño-4 region is partly attributed to the fact that there is a sharp decline in the number of events at higher threats in the western Pacific. The area averaged number of events in the Niño-4 decrease from 20 for threats=0 decreasing to just two for threats=1.0. The ROC curves for the last three-months (March-April-May) (not shown) of the forecasts show that the coupled model still possesses moderate skill ($A_{ROC} > 0.5$) out seven months.

Table 1. SST ROC Score

Threat=0	MM	MA	Threat=0.5	MM	MA	Threat=1.0	MM	MA
Niño-4	0.776	0.749	Niño-4	0.693	0.682	Niño-4	0.630	0.638
Niño-3	0.844	0.829	Niño-3	0.857	0.786	Niño-3	0.839	0.809
Niño-3.4	0.897	0.883	Niño-3.4	0.828	0.792	Niño-3.4	0.739	0.714

DJF precipitation ROC scores for four selected domains are shown in Table 2. Highlighted in **bold** are the higher values of the ROC. For all domains selected the MM has the higher skill (as measured by the ROC). Lack of skill ($A_{ROC} < 0.5$) exists in the Brazil domain for the MA for all precipitation threats. The Xie and Arkin (1997) monthly precipitation data set was used for the observations.

Table 2. Precipitation ROC Score

Threat=0.5	MM	MA	Threat=1.0	MM	MA	Threat=2.0	MM	MA
Southeast U.S.	0.582	0.555	Southeast U.S.	0.579	0.538	Southeast U.S.	0.567	0.512
Brazil	0.561	0.482	Brazil	0.549	0.480	Brazil	0.551	0.481
Northern Hemisphere	0.626	0.610	Northern Hemisphere	0.625	0.607	Northern Hemisphere	0.584	0.573
Tropical Pacific	0.735	0.707	Tropical Pacific	0.739	0.713	Tropical Pacific	0.713	0.707

This work is supported by NOAA grants NA76GP0521 and NA86GP00231.

Cocke, S. D and T. E. LaRow, 2000: Seasonal Predictions using a Regional Spectral Model Embedded within a Coupled Ocean Atmosphere Model. *Mon. Wea. Rev.*, **128**, 689-708.

Emanuel K. A., and M. Zivkovic-Rothman, 1998: Development and evaluation of a convective scheme for use in climate models. Unpublished manuscript.

Hogan, T. F., and T. E. Rosmond, 1991: The description of the Navy operational global atmospheric prediction system's spectral forecast model. *Mon. Wea. Rev.*, **119**, 1786-1815.

Krishnamurti, T., S. Low-Nam, and R. Pasch, 1983: Cumulus parameterization and rainfall rates II. *Mon. Wea. Rev.*, **111**, 816-828.

LaRow, T. E., and T. Krishnamurti, 1998: Initial Conditions and ENSO prediction. *Tellus*, **50A**, 76-98.

Moorthi, S., and M. J. Suarez, 1992: Relaxed Arakawa-Schubert: A parameterization of moist convection for general circulation models. *Mon. Wea. Rev.*, **120**, 978-1002.

Palmer T. N., C. Brankovic and D. S. Richardson 2000: A probability and decision-model analysis of PROVOST seasonal multi-model ensemble integrations. *Quart. J. Roy. Met. Soc.*, **126**, 2013-2035.

Pan, H-L., and W.S. Wu, 1994: Implementing a mass flux convection parameterization package for the NMC MRF model. Preprints, Tenth Conf. on Numerical Weather Prediction, Portland, OR, Amer. Meteor. Soc., 96-98.

Reynolds, R. W. and T. M. Smith, 1994: Improved global sea surface temperature analyses using optimum interpolation. *J. Climate*, **7**, 929-948.

Xie, P., and P. A. Arkin, 1997: Global Precipitation, a 17-year monthly analysis based on gauge observation, satellite observations, and numerical model output. *Bull. Amer. Meteor. Soc.*, **78**, 2539-2558.

Zhang, G. L. and N. A. McFarlane, 1995: Sensitivity of climate simulations to the parameterization of cumulus convection in the Canadian Climate Centre general circulation model. *Atmos. Ocean*, **33**, 407-446

Incorporating river routing in the Canadian Regional Climate Model

Philippe Lucas-Picher¹, Vivek K. Arora², Daniel Caya¹, and René Laprise¹

¹Département des sciences de la terre et de l'atmosphère, UQAM, Montréal, Québec, Canada.

²Canadian Centre for Climate modelling and Analysis (CCCma), Meteorological Service of Canada, University of Victoria, Victoria, British Columbia, Canada.

The framework for incorporating river flow routing in the Canadian Regional Climate Model (CRCM) is described. The incorporation of river routing in the CRCM will allow to simulate streamflow and model freshwater flux from the land surface to the ocean at the continental edges, which is an important contribution to ocean forcing.

The CRCM uses a semi-implicit, semi-Lagrangian scheme to solve the fully elastic non-hydrostatic Euler equations (Caya and Laprise, 1999) and, at its boundaries, may be driven by data from any general circulation model (GCM) or reanalyses. The horizontal resolution of the CRCM is approximately 45 km and it contains 30 levels in the vertical.

The discretization of major river basins at 5' resolution by Graham et al. (1999) is used as a template to define river basins at CRCM resolution. CRCM grid cells are assigned to major river basins as follows: (1) the 5' cells, corresponding to different river basins, lying within each CRCM cells are counted; (2) the CRCM cell is assigned to a river basin with the maximum number of 5' cells; (3) the resulting areas of the river basins at the CRCM resolution are compared with the original areas at 5' resolution, and any major discrepancy between these two areas is minimized by adding or subtracting CRCM cells to or from a given river basin. The region chosen for this study covers most of the North America (see Fig. 1). Graham et al. (1999) discretized 10 major river basins over North America and the discretization of these river basins at the CRCM resolution is shown in Fig. 1. The drainage areas of the major river basins at the CRCM resolution are compared with drainage areas based on 5' discretization of Graham et al. (1999) in Table 1.

Table 1: Comparison of drainage areas of river basins discretized at the CRCM resolution with drainage areas based on 5' discretization of Graham et al. (1999).

River Basin	Drainage area (km ²)		Percentage Difference
	Graham et al.	CRCM	
Mississippi	3,218,720	3,228,415	0.30
Mackenzie	1,735,635	1,748,230	0.73
Nelson	1,303,641	1,305,674	0.16
Columbia	1,106,969	1,106,439	-0.05
St-Lawrence	1,090,564	1,087,952	-0.24
Yukon	884,867	882,128	-0.31
Rio Grande*	856,547	149,144	-82.59
Colorado*	770,829	616,827	-19.98
Churchill	296,190	300,800	1.56
Fraser	262,854	260,419	-0.93

*The CRCM drainage areas for Colorado and Rio Grande do not compare well with Graham et al. (1999) values since these two river basins do not lie completely within the CRCM domain.

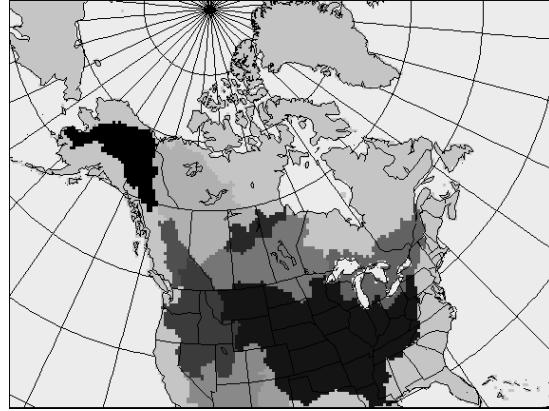


Figure 1: The domain of the CRCM shown in polar-stereographic projection. The discretization of major river basins (listed in Table 1) is shown in different shades of gray.

The river flow directions at the CRCM resolution are estimated using 5' flow directions obtained by Graham et al. [1999] and a methodology that requires minimal manual intervention (see Fig. 2). The original 5' flow directions were obtained by using mean elevations of the grid cells and assuming that the water drains in the direction characterized by the steepest slope. At spatial scales comparable to CRCM grid cells, the mean elevations of grid cells are not representative of their river flow directions. This is because rivers tend to flow in localized areas of low elevation, and the mean elevations of the grid cells are not representative of river bed profiles. Interpolation of 5' flow directions at the CRCM resolution is also difficult since the projection of CRCM is polar-stereographic, while the 5' flow directions are projected on a latitude-longitude grid. Therefore river flow directions are assigned to CRCM grid cells as follows: (1) the northern, eastern, southern, and western corners of the CRCM grid cell are identified; (2) these corners are used to outline a latitude-longitude grid box that encloses the CRCM grid cell; (3) a uniformly distributed unit amount of runoff is generated within this new grid box and allowed to find its way out of the box following the 5' flow directions; (4) the direction in which maximum amount of water is drained is identified; (5) by identifying the CRCM grid cell that receives this outflow, a river flow direction is assigned. Tests are made to ensure that flow continuity is maintained and that water does not flow between basins. The methodology used here for river basin discretization and obtaining flow directions is similar to the one used by Arora and Boer (1999).

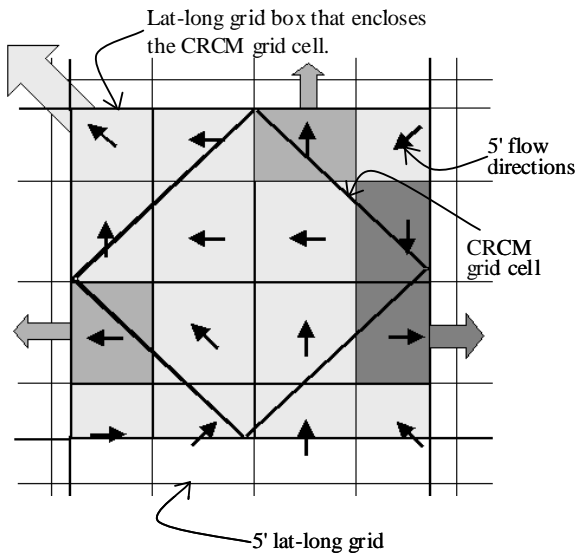


Figure 2: Methodology adopted to assign river flow direction to a CRCM grid cell. This CRCM grid cell, for example, was assigned the north-west direction because most of the 5' cells drain in this direction.

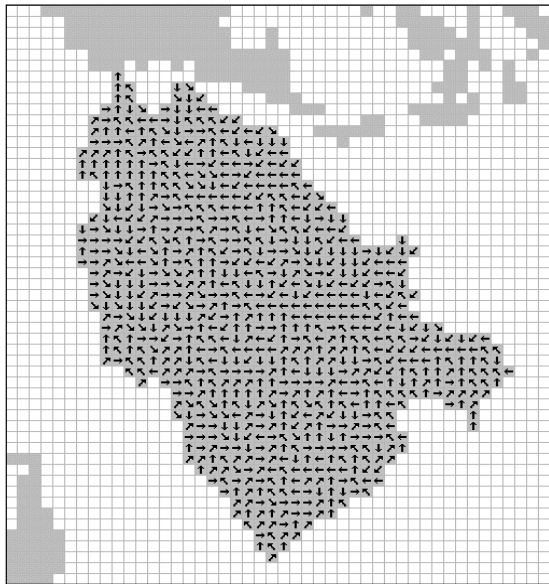


Figure 3: The river flow directions for the Mackenzie River basin at the CRCM resolution.

As an example, Fig. 3 shows the flow directions obtained for the Mackenzie River basin at the CRCM resolution using this methodology. Although tests are made to ensure the continuity of flow and that all grid cells eventually drain to the ocean, this does not ensure that the digital flow networks are realistic. The adequacy of digital flow networks is assessed by visually comparing the plots of river "order" with actual river networks. The grid cell where a stream originates is assigned an order 1.

The union of two streams of order n creates a stream of order $n+1$. Figure 4 shows the river order for land cells in the CRCM domain. Higher river orders are represented by darker shades. The digital river network shown in Fig. 4 compares well with the actual river network from atlases.



Figure 4: River order, which varies between 1 and 6 in this case, for the digital river networks obtained at the CRCM resolution.

The framework illustrated here is intended to be used with the flow routing scheme of Arora and Boer (1999) to obtain streamflow for 8 major North American Rivers. The Colorado and Rio Grande River basins are excluded since they do not lie completely within the CRCM domain. The simulated streamflow will allow assessment of the performance of the CRCM at river basin scales via comparisons with observed streamflow. This framework also gives the ability to assess the impact of climate change on streamflow. When runoff from control and enhanced greenhouse gas warming simulations of the CRCM are used as input into the flow routing scheme, the differences in simulated streamflow can be analyzed to assess possible impacts of change in climate on the hydrology of major North American rivers. These analyses are the subject of future research.

References

- Arora, V. K. and G. J. Boer, 1999, A variable velocity flow routing algorithm for GCMs. *J. Geophys. Res.*, 104, 30965-30979.
- Caya, D. and R. Laprise, 1999, A semi-implicit semi-Lagrangian regional climate model: The Canadian RCM. *Mon. Wea. Rev.*, 127, 341-362.
- Graham, S. T., J. S. Famiglietti and D. R. Maidment, 1999, Five-minute, $1/2^\circ$ and 1° data sets of continental water sheds river networks for use in regional and global hydrologic and climate system modeling studies. *Water Resour. Res.*, 35, 583-58.

Address any correspondence to Philippe Lucas-Picher (picher@sca.uqam.ca), Vivek Arora (vivek.arora@ec.gc.ca), Daniel Caya (caya.daniel@uqam.ca) or René Laprise (laprise.rene@uqam.ca).

Regional regimes with drought and extreme wet conditions: Possible changes in XXI century from IPSL-CM2 simulations

I.I. Mokhov, J.-L. Dufresne, V.Ch. Khon, H. Le Treut, V.A. Tikhonov

Obukhov Institute of Atmospheric Physics RAS, Moscow, Russia
Laboratoire Meteorologie Dynamique du CNRS, Paris, France

In this study we analyse possible regional changes of drought and extreme wet conditions in the XXI century relative XX century from simulations of a coupled atmosphere-ocean general circulation model (AOGCM) IPSL-CM2 with a carbon cycle for the 1860-2100 period (Friedlingstein et al., 2001; Dufresne et al., 2002). The IPSL-CM2 includes the LMD-5.3 AGCM (Le Treut and Li, 1991), the OPA-ice OGCM (Delecluse et al., 1993) and the OASIS coupleur (Terry et al., 1995). The carbon model includes the SLAVE code (Friedlingstein et al., 1995; Ciais et al., 1999) for the terrestrial part and the the IPSL-OGCM1 code (Aumont et al., 1999), based on the HAMOCC3 biochemical scheme (Maier-Reimer, 1993) for the ocean part. The scenario with the carbon dioxide emissions due to fossil and land use from observations up to 1990 (Andres et al., 1996) and the IPCC SRES98-A2 emission scenario from 1990 to 2100 (Nakicenovic et al., 2000) in these simulations were used.

There are different characteristics of drought and wet regimes. In particular, we analyzed model simulations of extremal meteorological conditions in May-July for the basic cereals-producing regions in the eastern European (EEP) and western Asian (WAP) parts of the former Soviet Union in comparison with observations from (Meshcherskaya and Blazhevich, 1997) for 1891-1995. In this case, for instance, the index D characterized the drought conditions with the negative precipitation anomalies ΔPr (normalized on the long-term mean value, MV, of precipitation) larger than -20% and positive temperature anomalies ΔT larger than 1K. The index W characterized the wet conditions with $\Delta Pr > 20\%$ and $\Delta T < -1K$. Two additional indices were also analyzed: D-W and $S = (\Delta T / \sigma_{\Delta T} - \Delta Pr / \sigma_{\Delta Pr})$, where $\sigma_{\Delta T}$ and $\sigma_{\Delta Pr}$ are respective standard deviations (SD).

There is a quite good agreement between model simulations and observations for SD of ΔPr (± 0.16 and ± 0.15) and for MV and SD of ΔT ($0 \pm 1.3^\circ C$ and $1.0 \pm 1.0^\circ C$) in the EEP. There is also good agreement in the WAP for MV of ΔT ($0^\circ C$ and $0^\circ C$) with a larger deviations for respective SD ($0 \pm 1.4^\circ C$ and $0 \pm 0.9^\circ C$) and for SD of ΔPr (± 0.10 and ± 0.17).

Model simulations reproduce quite well the dependence of ΔPr on ΔT for EEP ($dPr/dT = -0.06 \pm 0.01^\circ C^{-1}$ with coefficient of correlation $r=0.47$, while from observations $dPr/dT = -0.07 \pm 0.01^\circ C^{-1}$, $r=0.52$) for the period 1891-1995. The reproduction of this dependence for WAP is not so well (from observations $dPr/dT = -0.11 \pm 0.02^\circ C^{-1}$ with $r=0.58$, while no significant relation was found from model results).

Table 1 shows changes of different characteristics in summer between XXI and XX centuries from model simulations for East (EER: 46.1-53.2 °N, 39.4-50.6 °E) and West (WER: 46.1-53.2 °N, 0-11.2 °E) European regions. The D and M values characterize the portions (%) of total area under corresponding conditions during summer months. According to Table 1 model results display that the increase of temperature in the XXI century is accompanied in both regions by the decrease of precipitation and M and by the increase of D, D-M and S. It should be noted that changes in EER are not statistically significant. The appropriate changes in WER are more remarkable. Model simulations show the SD increase (in brackets) in the XXI century for temperature in both regions and for precipitation in WER, while the SD decrease for precipitation in EER. The drought indices display the general SD increase, while the wet conditions index M shows the SD decrease.

This work was supported by the CNRS/RAS Program and by the Russian Foundation for Basic Research.

Table 1.

Region	Century	T, °C	Pr	D, %	M, %	DM, %	S
EER	XX	0 (± 1.2)	1 (± 0.2)	3.6 (± 8.1)	3.0 (± 7.5)	0.6 (± 11.6)	0 (± 1.0)
	XXI	2.2 (± 1.5)	0.9 (± 0.2)	12.5 (± 13.1)	0.3 (± 2.0)	12.3 (± 13.5)	1.4 (± 1.0)
WER	XX	0 (± 0.9)	1 (± 0.1)	3.2 (± 6.4)	1.3 (± 4.5)	1.9 (± 8.0)	0 (± 0.7)
	XXI	2.9 (± 1.5)	0.8 (± 0.2)	30.2 (± 19.4)	0	30.2 (± 19.4)	2.4 (± 1.3)

References

1. Friedlingstein P., L. Bopp, P. Ciais, J.-L. Dufresne, L. Fairhead, H. LeTreut, P. Monfray, and J. Orr, 2001: Positive feedback between future climate change and the carbon cycle. *Geophys. Res. Lett.* V.28. No.8. P.1543-1546.
2. Dufresne J.-L., P. Friedlingstein, M. Berthelot, L. Bopp, P. Ciais, L. Fairhead, H. LeTreut, P. Monfray, J. Orr, 2002: Direct and indirect effects of future climate change on land and ocean carbon. *Geophys. Res. Lett.*
3. Meshcherskaya A.V., and V.G. Blazhevich, 1997: The drought and excessive moisture indices in a historical perspective in the principal grain-producing regions of the Former Soviet Union. *J. Climate.* V.10. P.2670-2682.
4. Le Treut, H., and Z.X. Li, 1991: Sensitivity of an atmospheric general circulation model to prescribed SST changes: feedback effects associated with the simulation of cloud optical properties. *Clim. Dyn.*, **5**, 175-187.
5. Delecluse, P., G. Madec, M. Imbard, and C. Levy, 1993: OPA version 7, Ocean General Circulation Model, Reference Manual., Tech. Rep., IPSL.
6. Terray, L., E. Sevault, E. Guilyardi, and O. Thual, 1995: The OASIS Coupler User Guide Version 2.0., Tech. Rep., CERFACS TR/CMGC/95-46.
7. Friedlingstein, P., I. Fung, E. Holland, et al., 1995: On the contribution of CO₂ fertilization to the missing biospheric sink. *Glob. Biogeochem. Cycles*, **9**, 541-556.
8. Ciais, P., P. Friedlingstein, D. Shimel, and P. Tans, 1999: A global calculation of the dC of soil respired carbon: Implications for the biospheric uptake of anthropogenic CO₂. *Glob. Biogeochem. Cycles*, **13**, 519-530.
9. Aumont, O., J. Orr, P. Monfray, G. Madec, and E. Maier-Reimer, 1999: Nutrient trapping in the equatorial Pacific: The ocean circulation solution. *Glob. Biogeochem. Cycles*, **13**, 351-369.
10. Maier-Reimer, E., 1993: Transport and storage of CO₂ in the ocean - an inorganic ocean-circulation carbon model. *Glob. Biogeochem. Cycles*, **7**, 645-677.
11. Andres, R., G. Marland, I. Fung, and E. Matthews, 1996: A 1° x 1° of carbon dioxide emissions from fossil fuel consumption and cement manufacture, 1950-1990. *Glob. Biogeochem. Cycles*, **10**, 419-429.
12. Nakicenovic, N., J. Alcamo, G. Davis, et al., 2000: IPCC Special Report on Emissions Scenarios. Cambridge University Press, Cambridge, United Kingdom and New York, NY, USA, 599 pp.

Dealing with atmospheric water in a nested RCM

Dominique Paquin and Daniel Caya
Université du Québec à Montréal
Département des sciences de la terre et de l'atmosphère.
paquin.dominique@uqam.ca

A nested Regional Climate Model, by definition, requires information from an external source. The needed initial and boundary conditions are generally provided by a GCM (General Circulation Model) for climate projections or by objectives analyses for current climate simulations. An implicit assumption in using a RCM stipulates that the atmosphere simulated by the regional model will follow the general state of the driven atmosphere. In other words, it is expected that a RCM will generate the high-resolution details without altering the large-scale atmospheric circulation. This implies that the large-scale means of the atmosphere should be similar in the RCM and in the pilot.

A complete RCM evaluation includes an estimation of the hydrological cycle, which is sensitive to the atmospheric water content. Differences in the pilot and in the RCM atmosphere will be reflected in the hydrological cycle and could modify the nested model humidity flux divergence.

To quantify the RCM and pilot humidity, an atmospheric water budget can be used. The budget equation takes the form of:

$$P - E = \quad (1)$$

$$-\frac{\partial r}{\partial t} - \nabla \cdot r\vec{V} - \frac{\partial c_w}{\partial t} - \nabla \cdot c_w\vec{V} - \frac{\partial c_i}{\partial t} - \nabla \cdot c_i\vec{V} + \varepsilon$$
where P is the total precipitation (large-scale plus convective), E the evaporation, r the water vapor mixing ration, c_w the cloud water, c_i the cloud ice and \vec{V} the horizontal wind. The residual term ε is introduced to

take into account errors from approximations in numerical formulation or interpolation.

Different deep convective parameterizations could be used to illustrate RCMs behavior regarding the atmospheric water content. Each convective parameterization follows particular triggering conditions and closure assumption, therefore modifying the humidity distribution and influences the hydrological cycle. The resulting atmosphere can differs from one type of parameterization to another.

To illustrate the topic, an experiment is conducted with the Canadian RCM (Caya and Laprise, 1999) and includes the atmospheric water budget computation. The CRCM is run for 4 months, from May to August 1988. The water budget is computed for JJA only, May being used for spin-up. The domain is centered over Texas and is composed of 141 x 121 grid points of 45 km of resolution, including a 9 grid points sponge zone, and is covering USA, Mexico and the surrounding sea. In the vertical, 18 levels up to 30 km in the atmosphere are used. The timestep is 15 minutes. ECMWF analyses of 2.5° resolution and 14 vertical levels provide the driving data every 12 hours. Two convective options are tested: the CGCMii moist adjustment scheme (McFarlane et al. 1992) and the Bechtold-Kain-Fritsch (BKF) (Bechtold et al. 2001) deep and shallow convective schemes. Table 1 provides the atmospheric water budget for every run as well as for the ECMWF driving data.

The dominant variables for every simulation are P, E and the water vapor divergence. (Over a period that is long enough the local rate of change of water vapor is less than the 3 dominant terms while the terms for cloud water and ice are always a few order less.) For the ECMWF analyses, there is positive divergence. In the CRCM with the GCMii moist adjustment scheme, the atmospheric water budget behavior is similar to the analyses and there is divergence of the water vapor flux. There is less precipitation than evaporation. The humidity lost over the domain has a source that is a draining from the soil water. However with the BKF' scheme have convergence of water vapor over the domain and more precipitation than evaporation.

Such differences in the atmospheric water budget are reflected in the time-series liquid soil water content presented on Fig. 1. The simulation using the moist adjustment has a total water decrease while the simulation with BKF shows a slight increase over the 4 months.

The simulations are too short to allow the model to reach equilibrium and to get final conclusions. This raises questions. The equilibrium value of the model atmospheric water value may differ between

CRCM simulation and the pilot. What are the implications? Is a RCM that has a mean atmospheric humidity profile that differs from the pilot able to simulate a reliable climate change projection? If the mean humidity profile of the atmosphere is different in a climate change context, will the RCM be able to capture the differences? These questions should be examined.

Table 1. JJA Water Budget ($\text{kg m}^{-2} \text{day}^{-1}$). \emptyset means that either the field is not available either the variable is not pronostic.

Experiment	P	E	$\frac{\partial r}{\partial t}$	$\nabla \cdot r\vec{V}$	$\frac{\partial cw}{\partial t}$	$\nabla \cdot cw\vec{V}$	$\frac{\partial ci}{\partial t}$	$\nabla \cdot ci\vec{V}$	ε
Moist adj.	2.59	2.79	0.08	0.26	\emptyset	\emptyset	\emptyset	\emptyset	0.14
BKF	3.60	3.27	0.07	-0.54	$\cong 0$	$\cong 0$	$\cong 0$	$\cong 0$	-0.13
ECMWF	\emptyset	\emptyset	0.14	0.40	\emptyset	\emptyset	\emptyset	\emptyset	\emptyset

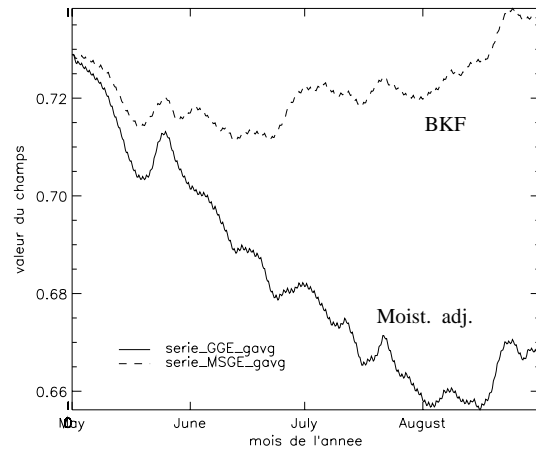


Figure 1. Time series grid-averaged liquid water soil content (%).

Bechtold, P., E. Bazile, F. Guichard, P. Mascart and E. Richard, 2001: A Mass Flux Convection Scheme for Regional and Global Models. *Quart. J. Roy. Met. Soc.*, **127**, 869-886.

Caya, D. and R. Laprise, 1999: A semi-implicit semi-Lagrangian regional climate model: the

Canadian RCM. *Mon. Wea. Rev.*, **127**, 341-362.

McFarlane, N. A., G. J. Boer, J.-P. Blanchet and M. Lazare, 1992: The Canadian Climate Centre Second-Generation General Circulation Model and its Equilibrium State. *J. Clim.*, **5**, 1013-1044.

Statistical Analysis of Interannual Arctic Sea Ice Modeling.

V.P.Parkhomenko

Computing Centre of the Russia Academy of Sciences

Vavilov Str. 40 Moscow 117967 Russian Federation

E-mail: parhom@ccas.ru

The application of AGCM, ocean hydrothermodynamical model and sea ice evolution model to Arctic region is discussed.

The sea ice model is based on Semptner and Hibler model. Ice compactness, presence of thick and thin ice in a cell, snow mass in ice cell, specific ice melting and producing processes are taken into account. The purpose of the work is analysis of seasonal and annual evolution of sea ice, long-term variability of a model ice cover, and also its sensitivity to some model characteristics.

The numerous experiments according to influence of some model parameters on results are carried out. Ice and snow albedo and ocean heat flux in ice are most important in this connection.

Results of 70 years simulation of Arctic basin sea ice evolution are analyzed. The average ocean currents data are taken from observations. Ice thickness for a cell with coordinates 170W, 86N depending on time are submitted in Fig. 1. The separate points define daily average meanings. 365 days moving average is shown by a thick line. The significant (about 0.5 m) interannual fluctuations of an ice cover exist. The spectral analysis of results allows to make exacter conclusions about the ice cover change in time. Periodogram, determining amplitudes of spectral decomposition harmonics of ice thickness in the specified cell, is shown in a Fig. 2. The basic peak, naturally, corresponds to a one year (365 days) period. There are also rather appreciable fluctuations with a 5 years period and further continuous wide spectrum with periods more than 10 years. The Fig. 3 shows periodogram for the same variable, but when annual and seasonal components are excluded. The diagram shows, that there are only synoptical fluctuations with a 3 - 10 days period and of rather small amplitude. The auto correlation function with the excluded annual and seasonal components (Fig. 4) shows data dependence with 3 days time lag. The similar results are received for other points, and also for average ice thickness in Arctic Region. There are significant interannual fluctuations of sea ice cover with periods in 4 - 5 years.

This work is supported by RFFI.

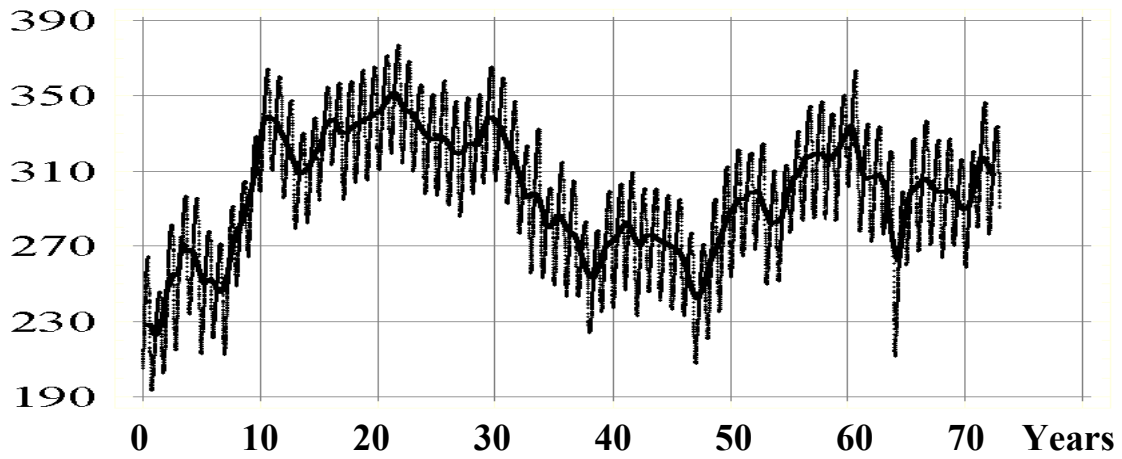


Fig. 1. Sea ice thickness (m).

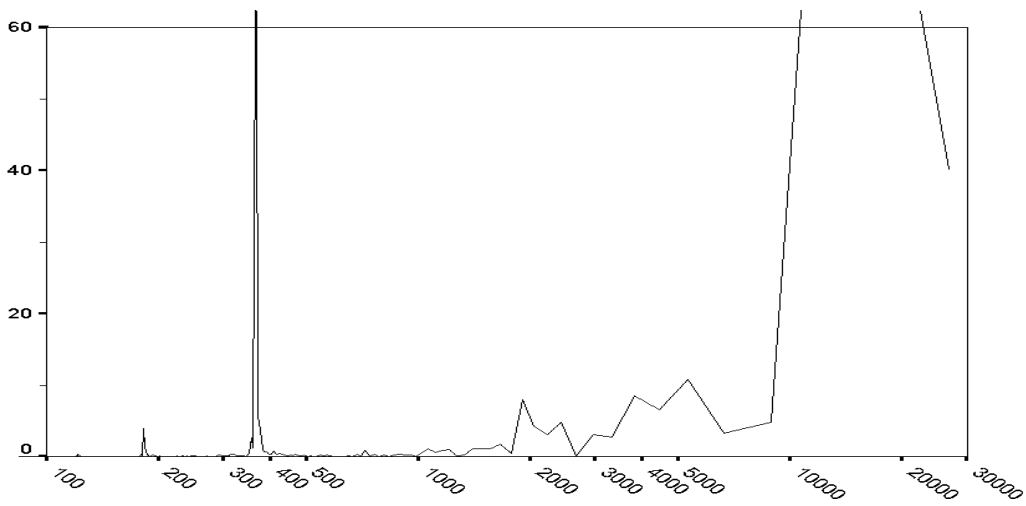


Fig. 2. Periodogram for sea ice thickness. Period in days.

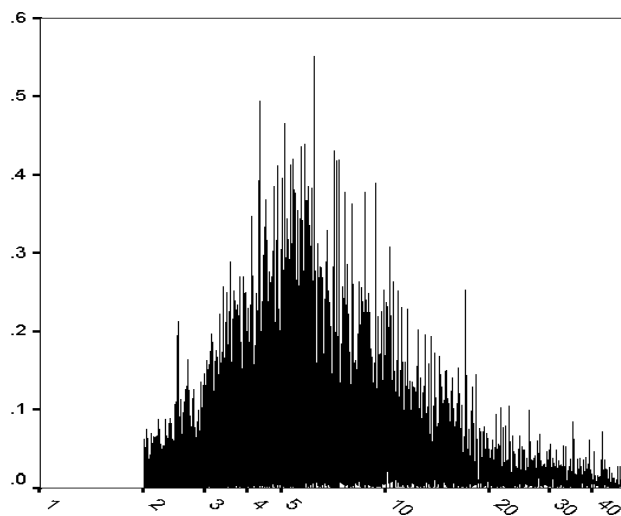


Fig. 3. Periodogram for sea ice thickness. Period in days. Excluded seasonal cycle.

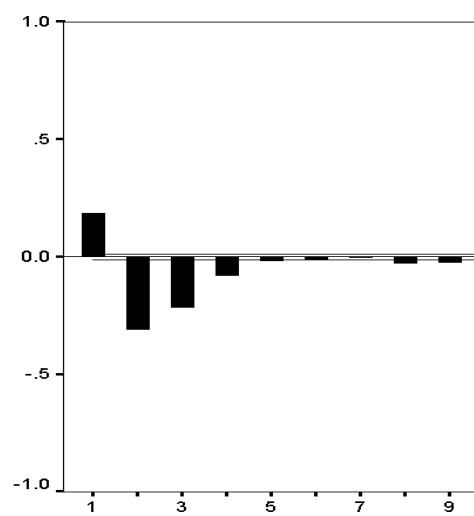


Fig. 4. Autocorrelation. Time lag – days.

Assessing the performance of statistical downscaling setups in Cameroon

Edouard K. Penlap^{1,2} and Christoph Matulla^{1,3}

¹Institute for Coastal Research, GKSS Research Centre, Max-Planck-Straße, 21502 Geesthacht, Germany

²Atmospheric Sciences Lab, Dep. of Physics, Faculty of Sciences, University of Yaounde I, Cameroon

³Institute of Meteorology and Physics, University for Agricultural Sciences, Vienna, Austria
email: penlap@gkss.de

The purpose of this study is to estimate the response of local precipitation in Cameroon to external climate forcing as simulated by general circulation models (GCMs). This will be done by using linear and non linear statistical methods. The achieved results can also serve as a lower bound for the performance that should be obtained by regional climate models (RGMs). Camerouns climate runs from humid-equatorial close to the Atlantic ocean to arid-tropical in the vicinity of the lake Tchad, which belongs to the Sahelian zone. Hence precipitation varies intensively in space as well as in time. Thus Cameroon can be indicative of different African climates. This signifies also a strong challenge for the used methods. For brevity after a superficially description of the local climate and data only some preliminary results concerning canonical correlation analysis (CCA) are presented. One goal of further investigations will be to study the impacts of the IS92 and SRES scenarios, calculated by the ECHAM4/OPYC3 climate model.

Comments on the Climate

Cameroon is situated at the Gulf of Guinea, close to the Equator, in Central Africa and its climatic situation is complex due to several reasons: • It lies inside the Inter-Tropical-Convergence-Zone (ITCZ). Thus rainfall is dominated by two air flows, Harmattan and Monsoon, which hail from the Azores and Sainte-Hélène anticyclones respectively. Harmattan and Monsoon meet along the Inter-Tropical-Front line (ITF), whose latitude varies within the year. • Due to its proximity to the Atlantic local rainfall is strongly affected by the ocean. Even Sahelian rainfall is influenced by sea surface temperature (Wassila et al. 1999). • The mountain chain of West-Cameroon divides the country in two parts and thereby influences the rain patterns.

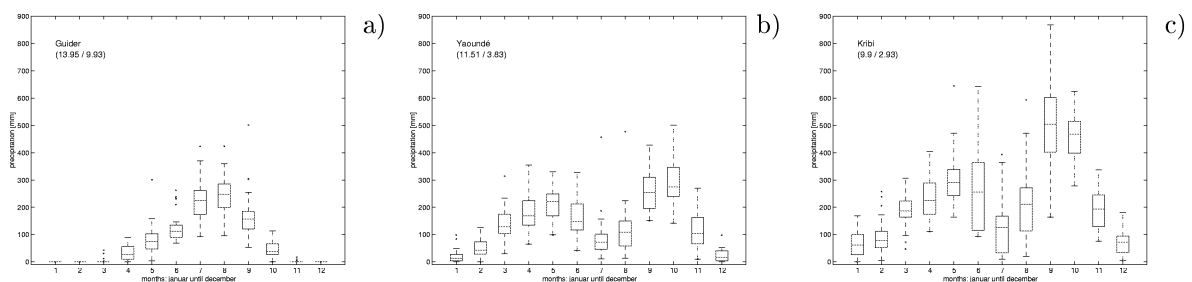


Figure 1. The panels show boxplots of representative stations.

Hence Camerouns climate is equatorial-tropical in coastal regions, semiarid in the Adamaoua plateau and arid next to lake Tchad. Three climatological rainfall regimes can be clearly identified (Kamga 2001): (i) the Sahelian climate with less than 400mm annual rain, (ii) the tropical climate with yearly totals between 400 and 1500mm and (iii) the sub-tropical climate with annual rainfall between 1500 and 4000mm (see Figure 1. a, b and c respectively).

Therefore Cameroon is a good candidate for studying different African climates and to examine the capability of the statistical models under variable conditions.

Data

1. For fitting and validating the different statistical models we consider the period from 1951 to 1990. As predictors we use monthly mean SLP, SST and surface-wind taken from the National Center for Environmental Prediction (NCEP) and the National Center for Atmospheric Research (NCAR) reanalysis (Kalnay et al. 1996). Spatial resolution is about 250 km. We choose the sector from 10°W to 20°E and 20°S to 20°N.
2. On the regional scale 33 monthly mean precip. records are used (Figure 2.). Figure 1. shows the precip. statistics of stations characteristically for the different climatic regions in Cameroon (Guider, Yaounde and Kribi).
3. Predictors for the small-scale precip scenarios and the first half of the 21 century are extracted from the ECHAM4/OPYC3 IPCC scenario-realizations (Roeckner et al. 1996).

Results and Outlook

Different statistical methods will be applied - canonical correlation analysis (CCA), singular value decomposition (SVD) and multiple linear regression (MLR). These techniques are wellknown and mathematical background can be found in i.e. von Storch and Zwiers (1999). Presented results refer only to CCA, as the calculation using other methods has not been done yet. The results refer to greater rainy season August, September, October (ASO) with SST as large scale predictor.

We apply CCA after a transformation in empirical orthogonal function (EOF) coordinates. The first step is to analyse the observed data by means of EOF analysis and separate the signal from the noise. On the basis of scree-plots we decided to retain four EOFs (94%) on the large- and seven (70%) on the small-scale. The leading local EOF (almost 20% of explained variance) appears to divide Cameroon into three regions (Figure 2.a). One with latitudes more than 7°N, one south of the Adamaoua plateau and the coastal region. This is in agreement with local topography. In the latter two regions the variance explained by the associated principal component reaches a flat maximum.

The first large scale EOF (not shown) explains 63% of the variance. CCA produces pairs of patterns that maximize the correlation of the canonical series. Figure 2. b), c) show the first pair of patterns.

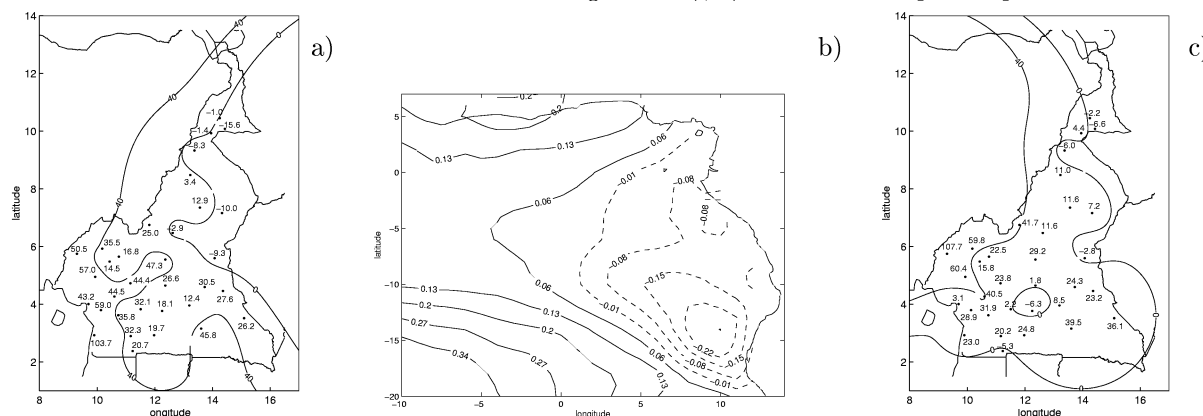


Figure 2. a): the first local EOF; b) and c): the first pair of canonical correlation patterns of observed SLP and simultaneous Cameroon precipitation anomalies. The correlation between the corresponding timeseries is 0.7. The SST [°C] (rainfall [mm/month]) pattern explains 13% (21%) of the variance. Circles indicate the stations.

To assess the performance of the method the datasets are used in the following way: period - 1951/80 for model fitting and the total for validation. CCA is applied to August, September, October separately and the whole season (ASO). The results are displayed in Figure 3. Boxplots show the behaviour of the significant correlation coefficients (more than 95%) between estimation and observation at all stations. Figure 3 g) shows the highest correlation reached (a star indicates August, + September, . October and o the seasonal mean ASO). This might give an impression of the complexity of Cameroon rainfall. The achieved correlations demand further work. Apart from the distinction of local regions the influence of different large scale sectors is to be examined. Thus, beside the application of other methods and predictors we will also consider different regions and more sectors.

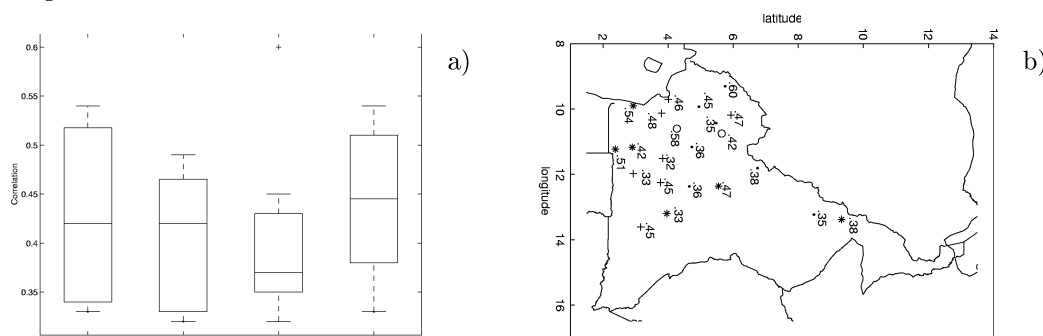


Figure 3. a) model performance for August, September, October and the seasonal mean (ASO) (no distinguishing between local regions); b) the highest performance at individual stations that can be attained with the used setup (August:*,September:+,October:.,saisonal mean:o)

Kalnay, E., M. Kanamitsu, R. Kistler, W. Collins, D. Deaven, L. Gandin, M. Iredell, S. Saha, G. White, J. Woollen, Y. Zhu, M. Chelliah, W. Ebisuzaki, W. Higgins, J. Janowiak, K.C. Mo, C. Ropelewski, J. Wang, A. Leetmaa, R. Reynolds, R. Jenne, and D. Joseph, 1996: The NCEP/NCAR reanalysis project.. *Bull.Amer.Meteor.Soc.*, **77**, 437-471.

Kamga, F.M., 2001: Impact of greenhouse gas induced climate change on the runoff of the Upper Benue River (Cameroon). *Journal of Hydrology*, **252**, 145-156.

Roeckner, E., J. Oberhuber, A. Bacher, M. Christoph, and I. Kirchner, 1996: Enso variability and atmospheric response in a global coupled atmosphere-ocean gcm. , **12**, 737-745.

von Storch, H., and F. Zwiers, 1999: *Statistical Analysis in Climate Research*. Cambridge University Press, 484 pp.

Wassila, M., G.A. Barnston, and K. Vadlamani, 1999: Prediction of African rainfall on the seasonal timescale. , **104**, 31589-31597.

Sensitivity of short simulations to the various parameters in the new CRCM spectral nudging

Sébastien Riette and Daniel Caya¹

UQÀM: Département des sciences de la terre et de l'atmosphère

CP 8888, Succ. "Centre-Ville", Montréal, Québec, Canada, H3C 3P8

1) Introduction and experimental design

The basic idea behind the use of Regional Climate Models (RCM) to downscale outputs of Global Circulation Models (GCM) consists in adding high-resolution details on the GCM large-scale flow without altering long waves. However, for particular circulation patterns, the Davies (1976) approach used in most RCMs to specify their lateral boundaries over a given sponge zone is insufficient to insure the coherence between the large-scale circulations of the driving and driven models. To correct this problem in the Canadian RCM (CRCM, Caya and Laprise, 1999), a spectral nudging (Biner *et al.*, 2000) of the large-scale wind was applied over the whole model domain in addition to the Davies' specifications of the lateral boundaries. The filter used by Biner *et al.* (2000) to select the large-scale part of the circulation was quite crude and cannot accurately select the wanted scale. However, the proof of concept was made and their spectral nudging prevented the CRCM simulation from drifting from its driving data. A new version of the spectral nudging in the CRCM was developed using a more sophisticated spectral filter based upon cosine functions (Denis *et al.*, 2001). The experiment reported in this paper aims at defining the adjustable parameters of the CRCM spectral nudging in order to minimize the strength of the forcing while keeping the large-scale circulation of the nested model coherent with its counterpart from the driving data. The adjustable parameters in the new version of the CRCM spectral nudging are: the wavenumber of the shortest wave that is included in the nudging procedure, the intensity of the nudging and the vertical profile of the nudging. The spectral nudging is only applied to the top most levels of the model with an increasing value as we go upward in altitude. In this short note, only the number of waves required in the nudging and its intensity at the top level is investigated.

Simulations were performed on a 96*96 points polar-stereographic grid covering the continental US. The distance between gridpoints is 60 km in the horizontal using a 900 s timestep and there are 15 vertical levels up to about 20 km. Simulations are 15-day long initialised on May 15th 1988 at 00 GMT. Initial and boundary conditions are taken from 2.5° NCEP analyses. The second half of May was selected because of a large-scale closed low-pressure system that is totally missed by the CRCM when the regular Davies nesting is used. This results in RMS difference between CRCM and NCEP 250 hPa geopotential that remains large for 4 days. The spectral nudging keeps the CRCM large-scale flow close to its driving data.

2) Sensitivity to the shortest wave included in the nudging

Different experiments are made to establish the shortest wave that must be nudged to keep the CRCM large-scale circulation similar to the driving one. In order to keep the CRCM ability in developing the high-resolution details of the flow, the nudging must be limited to long waves.

In order to assess the shortest wave needed, the difference between the CRCM and NCEP 250 hPa kinetic energy is computed for a spectral nudging using an increasing number of waves starting with the fundamental. Figure 1 shows that nudging only wave number 1 has a very weak influence on the RMS difference. The insertion of waves 2, 3, 4 and 5 in the nudging decreases the RMS difference and peaks disappear with the nudging of wave 4. There is no additional reduction of the RMS difference after wave 5 is included. Therefore it seems that nudging the four longest waves (from 1450 km to 5750 km) are needed to anchor the CRCM large-scale circulation to its driving data.

Supplemental experiments were made and the results show that nudging smaller waves doesn't improve the simulation and have negative effects by reducing the variance of smaller waves simulated by the CRCM.

3) Sensitivity to the intensity of the nudging

The intensity of the forcing is not uniform in the vertical keeping the model as free as possible in the low levels. Therefore, the spectral nudging is null from the surface to a given level (adjustable) and then, increases with altitude to reach its maximum value (adjustable) at the top of the model. The sensitivity of the model to this maximum value is investigated.

¹ caya.daniel@uqam.ca

Experiments are made with a maximum value of 1, 0.5, 0.25, 0.2, 0.15 and 0.1 (where for example, 0.25 is the weight of the driving data used in the computation of the CRCM long waves at the topmost level). The same diagnostics are presented for these new simulations. Figure 2 shows that an intensity of 0.1 seems sufficient to reduce the RMS difference to an acceptable value but inspection of the simulated fields (Figure 3) made evidence for using a value of 0.2. Various simulations were then performed to select the level from which the nudging is applied and results showed that the model is almost insensitive to this parameter when varying from 500 hPa to 900 hPa.

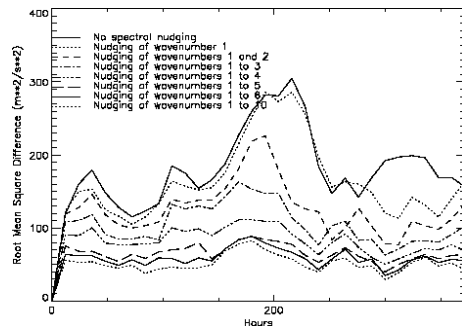


Figure 1. Time series of domain averaged RMS difference between CRCM and NCEP 250 hPa kinetic energy for various waves nudged.

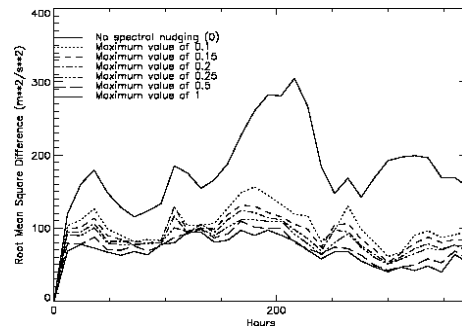


Figure 2. Same as figure 1 but for various maximum values of the spectral nudging strength.

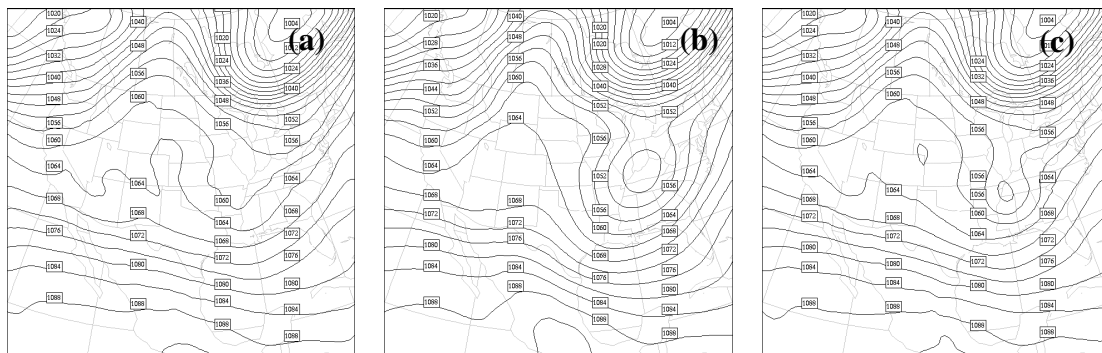


Figure 3. 250 hPa geopotential height on 24 May at 12 GMT for (b) the NCEP analysis and for the CRCM with (a) 0.1 or (c) 0.2 as maximum value for the spectral nudging.

4) Conclusion

A set of simulations was generated to select the wave that have to be retained, the maximum intensity and its vertical profile in the new CRCM spectral nudging. From these simulations, it has been found that wave 1 to 4 need to be included in the nudging with a weak maximum value of 0.2 applied at the top level of the model. The model appears to be quite insensitive to the location of the lowest level to be nudged when chosen between 500 hPa and 900 hPa. However, these tests were performed over a single grid, for short simulations and for a given set of objective analyses. More thorough experiments are needed to infer the complete behaviour of the new spectral nudging scheme.

Moreover, it should be kept in mind that the spectral nudging is not physical and should be kept to much weaker value than what is present in the dynamic and the physic of the model. Results from this study are in this direction but a comparison of the amplitude of the various forcings is required.

References

- Biner, S., Caya, D., Laprise, R. and Spacek, L. (2000). Nesting of RCMs by imposing large scales. *Research activities in atmospheric and oceanic modeling*, 30:7.3
- Caya, D. and Laprise, R. (1999). A semi-implicit semi-lagrangian regional climate model: the canadian RCM. *Monthly Weather Review*, 127:341-362
- Davies, H. C. (1976). A lateral boundary formulation for multi-level prediction models. *Quart. J. R. Met. Soc.*, 102:405-418
- Denis, B., Côté, J. and Laprise, R. (2001). Spectral decomposition of two-dimensional atmospheric fields on limited-area domains using the discrete cosine transform (DCT). *Accepted to Monthly Weather Review*.

Modelling of Atmospheric Angular Momentum in a simple AGCM

Oliver Stenzel* and Jin-Song von Storch
Meteorological Institute, University of Hamburg, Germany

Introduction

This work investigates the impacts of various large-scale thermal forcings on the global AAM. The investigation is based on numerical experiments with a simple GCM, PUMA (Portable University Model of the Atmosphere) [Fraedrich et al., 1998]. The non-linear hydrodynamics of the atmosphere are represented in PUMA in the same way as in a standard GCM, but the latitude-dependent radiative forcing is strongly simplified and expressed as a Newtonian cooling $F_R = \frac{T_R - T}{\tau_R}$, where F_R is the forcing, T_R is the restoration temperature and τ_R the e-folding time of the Newtonian cooling. By modifying the restoration temperature field, the large-scale thermal forcing of the atmosphere can be easily controlled.

A series of numerical experiments are carried out using different restoration temperature fields and orographies. The restoration temperature fields are zonally symmetric and have different meridional gradients. It is found that the global AAM increases with increasing meridional gradient in the thermal forcing. The increase in the AAM is characterized by a change in circulation regime in the mid- and high-latitudes: The structure of the transients changes from a zonal wavenumber six to three, and the number of cells in the meridional circulation reduces from three to two with a diminishing polar cell.

The ΔT -Experiment

An experiment is conducted to investigate the dependencies of AAM on the mean meridional temperature gradient. In this experiment the meridional gradient of the restoration temperature field is increased by steps of 10K from $\Delta T = T_R(EQ) - T_R(POLE) = 0$ to $\Delta T = 190K$. For each of these configurations the model is integrated over ten years. As it is to be expected, the AAM grows with increasing ΔT (Figure 1a). But unlike the total kinetic energy KE (Fig. 1b) the function of AAM is not “smooth”. It shows three nearly linear regions which are divided by ranges of a remarkably smaller slope. This behavior arises from changes in the mid- and high-latitude circulation regimes.

The first region is a global Hadley-regime (not shown here). The second one is a Rossby-regime during which the mid-latitude eddies are growing in size and strength. For stronger meridional restoration temperature gradients ($\Delta T \geq 120K$) the eddies begin to extend pole-ward and a different Rossby-regime is formed with low pressure over the poles and huge anticyclones in the mid-latitudes. The change from regime 2 to regime 3 can be seen in the meridional mass-stream-function (Fig. 2) as well as in the shift of the predominant wave number of synoptic activity from six to three (Fig. 3).

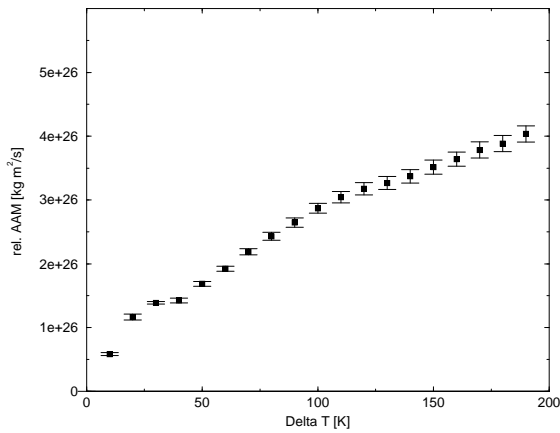
So how do these transitions of circulation patterns affect the AAM? To answer this, one can look at the ratio of eddy kinetic energy to total kinetic energy EKE/KE (Fig. 1b). The EKE is, as well as the KE, a monotonically growing function of ΔT . However the ratio of both is not. As long as the eddies are growing, the EKE’s share of KE is growing too. So a smaller part of the growing KE is zonal mean kinetic energy KZ. After entering the third regime, KZ can hold its share of KE and the AAM grows faster again, though not as fast as in regime 2.

We continue our work with the investigation of transient and abrupt changes in the restoration temperature fields and experiments with real and idealized orographies.

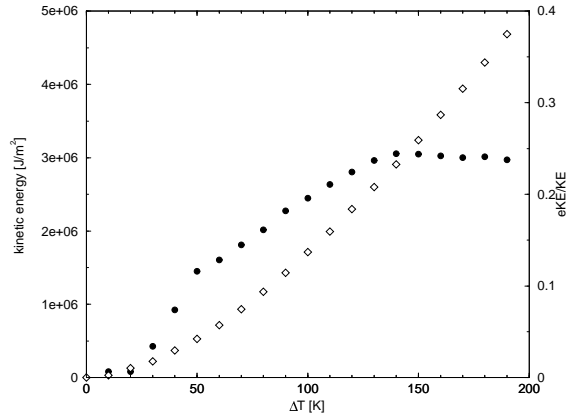
References

Klaus Fraedrich, Edilbert Kirk, and Frank Lunkeit. Portable university model of the atmosphere. Technical Report 16, Deutsches Klimarechenzentrum, 1998.

*contact address: stenzel@dkrz.de

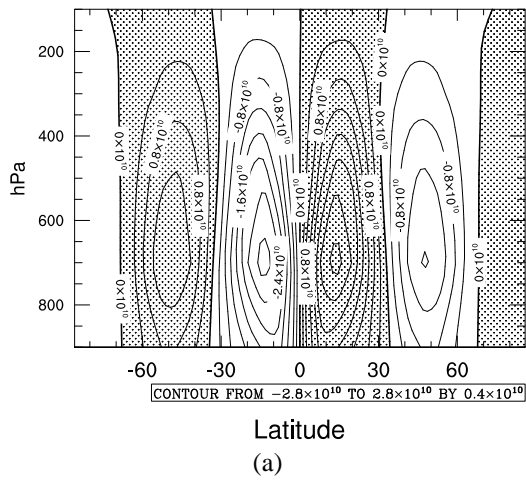


(a) Relative angular momentum.

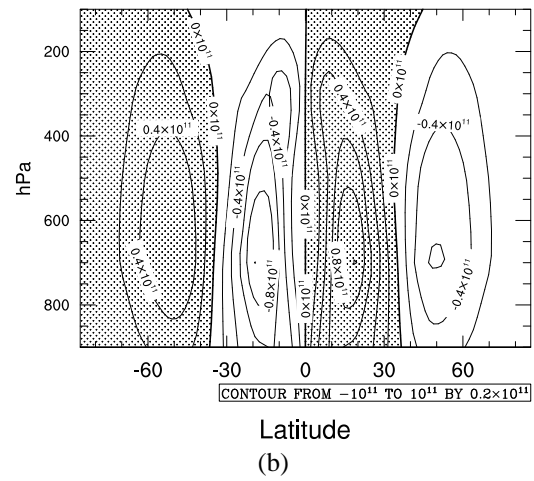


(b) Total kinetic energy KE (open diamonds) and ratio EKE/KE (filled circles).

Figure 1: Relative angular momentum and kinetic energy



(a)



(b)

Figure 2: Meridional mass-stream-function for (a) $\Delta T = 60K$ and (b) $\Delta T = 180K$ given in kg/s .

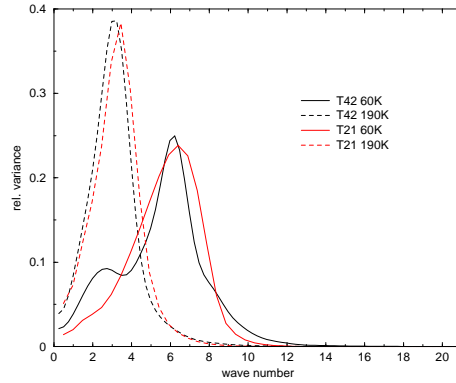


Figure 3: Wavenumber spectrum derived from the surface pressure along $45^\circ N$. The maximal variance is located at wavenumber 6-7 for $\Delta T = 60K$ but shifts to wavenumber 3 for $\Delta T = 190K$. The robustness of this result is checked by performing the same experiment with PUMA at T21 and T42 truncation.

Climate Variability within the climate model ECHO-G during the Dalton Minimum

Sebastian Wagner

Institute for Coastal Research, GKSS-Research Centre, Germany*

February 21, 2002

Introduction

Due to the lack of historical climate data around the world prior to the mid-19th century, climate model simulations are used to study climate in the past in a global context. In this study the output of the climate model ECHO-G is analysed concerning the climate variability during a time with reduced solar activity and enhanced volcanic activities at the beginning of the 19th century, known as the Dalton Minimum. The climate model ECHO-G constitutes of the atmospheric model ECHAM4 (T30-resolution) and the global ocean circulation model HOPE-G (T42-resolution), both developed at the MPI in Hamburg. The model is forced with solar irradiance and volcanic dust indices as well as with greenhouse gas concentrations in order to simulate external conditions of the past in an appropriate way (Fig. 1).

Winter temperatures

The averaged winter temperatures during the period 1700-1990 are given in Figure 2. The northern hemisphere north of 30°N reveals an increased temperature range compared to the tropics and the southern hemisphere south of 30°S. This is due to the relatively huge continental influence on the northern hemisphere. Furthermore the temperature in this part of the globe shows a marked resemblance to the external forcing, whereas the southern hemisphere deviates in some periods. Within the first part of the Dalton Minimum there is also a marked contrast in the temperature development on both hemispheres with cooling in the northern hemisphere and the tropics and a warmig tendency in the southern hemisphere. This trend is reversed after 1810 when temperatures in the southern hemisphere eventually also decrease. Another interesting fact between the external forcing and temperature is the time lag between the minimum of the solar activity around 1815 and the minimum of the temperatures around 1840. This phenomenon probably involves a lagged oceanic response to the external forcing.

In the section above only averaged temperatures are analysed. A question further to discuss is the regional - or continental - temperature impact. Figure 3 shows the leading EOFs of northern hemisphere winter temperatures (T2m) and sea level pressure (SLP) north of 30°N together with their Principal Components (PC) explaining 16% and 27% of total T2m and SLP variance, respectively. EOF 1 T2m shows the seesaw between Eurasia and Greenland as well as between central North America and Alaska. The PC of EOF 1 T2m reveals that during certain periods within the Dalton Minimum above normal temperatures prevail in Greenland and Alaska. The first SLP-EOF is connected to the Arctic Oscillation (AO). The SLP-PC indicates negative values or values close to zero connected with weak or inverse AO during the Dalton Minimum. A physical explanation for this phenomenon is probably the reduced temperature gradient between high and low latitudes due to reduced solar irradiance. This leads to an enhanced meridional circulation due to weakened zonal winds as seen in PC 1 of SLP.

Acknowledgements

The whole 500-year simulation was carried out at the German Climate Computing Centre (DKRZ) by F. Gonzalez and E. Zorita (both GKSS) and U. Schlese (DKRZ). The forcing data for the integration were kindly supplied by T. Crowley (Texas University).

*Corresponding author address: GKSS-Forschungszentrum, Max-Planck-Str.1, 21502 Geesthacht, Germany; e-mail: swagner@gkss.de

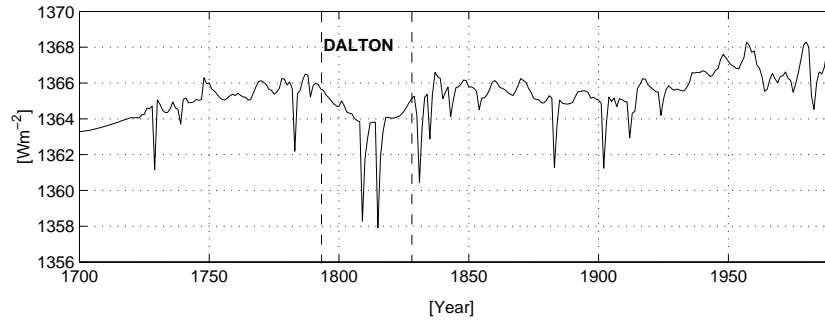


Figure 1: Solar and volcanic climate forcing from 1700-1990. The Dalton Minimum lasts from 1790-1840 with volcanic eruptions, e.g. Tambora 1815.

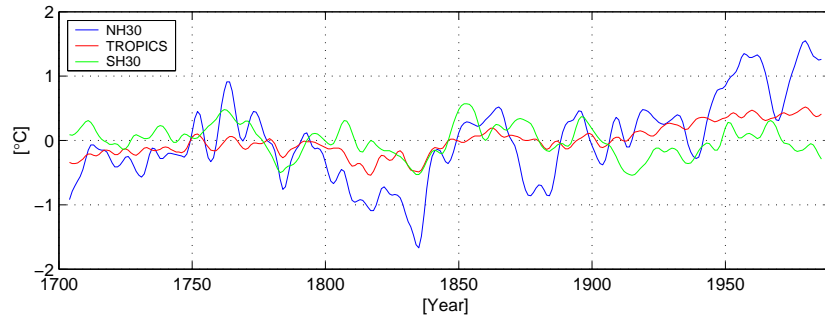


Figure 2: Winter temperature anomalies 1700-1990 in the northern (NH30) and southern hemisphere (SH30) north and south of 30° , respectively, and the tropics smoothed with a 10 years Gaussian filter. Notice the strong resemblance of NH30 temperatures with the external forcing as well as the time lag to the external forcing at the time of the Dalton Minimum.

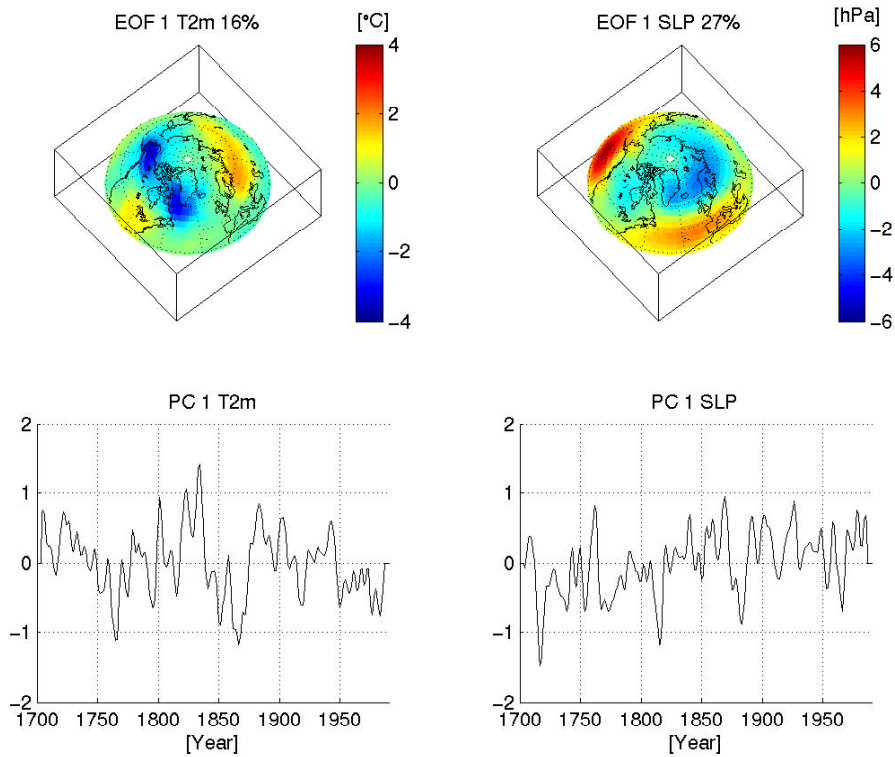


Figure 3: Leading EOFs of temperature and sea level pressure and appendant Principal Components (PC) for the northern hemisphere north of 30°N smoothed with a 10 years Gaussian filter. Notice the regional different temperature impacts due to atmospheric circulation anomalies.

Reconstructing Australian environments of the last glacial cycle through quantitative modelling

Richard Wardle and Ian Simmonds

School of Earth Sciences
The University of Melbourne
Parkville, Victoria
Australia, 3052
Email: rwardle@unimelb.edu.au

Our work involves the systematic study of large-scale changes in global climate and regional changes for the Australian continent that have occurred over the last 130,000 years. There currently exists a need for the interpretation of the data based reconstructions within a dynamical framework. Our modelling approach will provide simulated climate and hydrological model data sets with which to compare the reconstructed climates, identifying consistencies and inconsistencies that may exist with the dynamics.

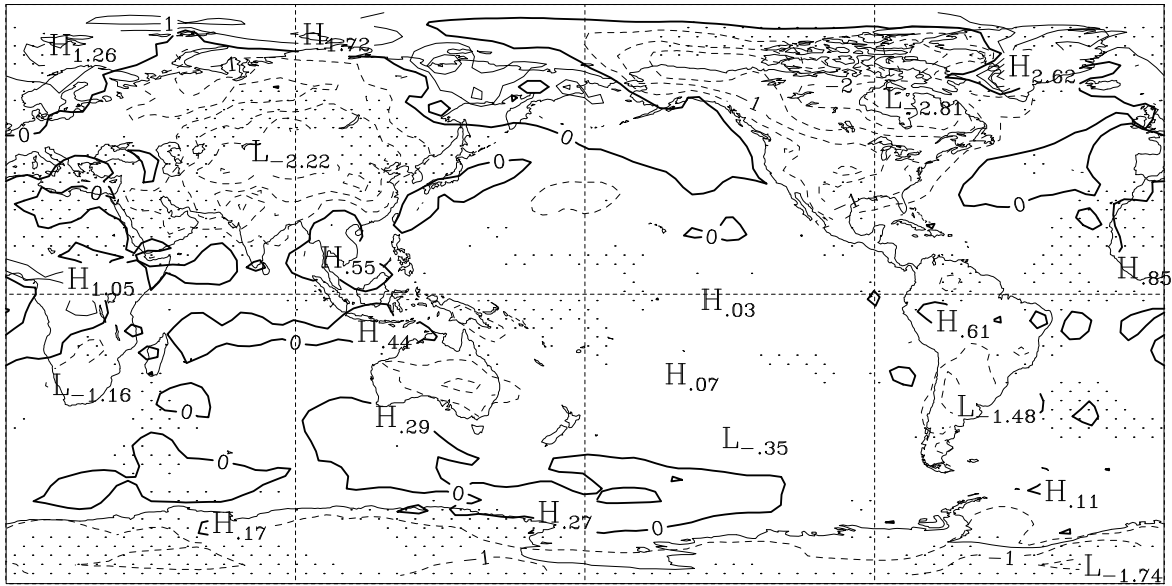
The global simulations are performed with a sophisticated atmospheric GCM which successfully replicates the present day (PD) climatology. Focus will then turn to smaller scales within Australia, where limited area models and hydrological models will be used to understand processes down to the catchment level. We focus initially on the mid-Holocene (6 ka), an epoch for which relatively large amounts of paleo data exist and for which there is a clear understanding of the climate forcings. Boundary conditions are consistent with the Paleoclimate Modelling Intercomparison Project (PMIP) with only the orbital forcings and atmospheric CO₂ concentrations differing from those of today.

The model simulated DJF surface air temperature anomalies (6ka - PD) shows cooler temperatures for most of the land masses over the globe (Fig. 1a). Statistical significance at the 95% level is indicated by stippling. Fig. 1b shows the corresponding JJA distribution. Australia is marked by reduced seasonality, in contrast to the northern hemisphere where summers are warmer and winters colder. Reconstructed paleo vegetation maps through proxy methods yield a mid-Holocene Australian climate that, with a few notable exceptions, is similar to today [Dodson (1992)]. The palynological data [Kershaw *et al.* (1991), Kershaw *et al.* (2000), among others] suggest that the conditions in Australia at that time were up to 25% wetter than today with warmer annual mean temperatures of about 1°C concurrent with reduced seasonality, in agreement with the climate simulated by the model.

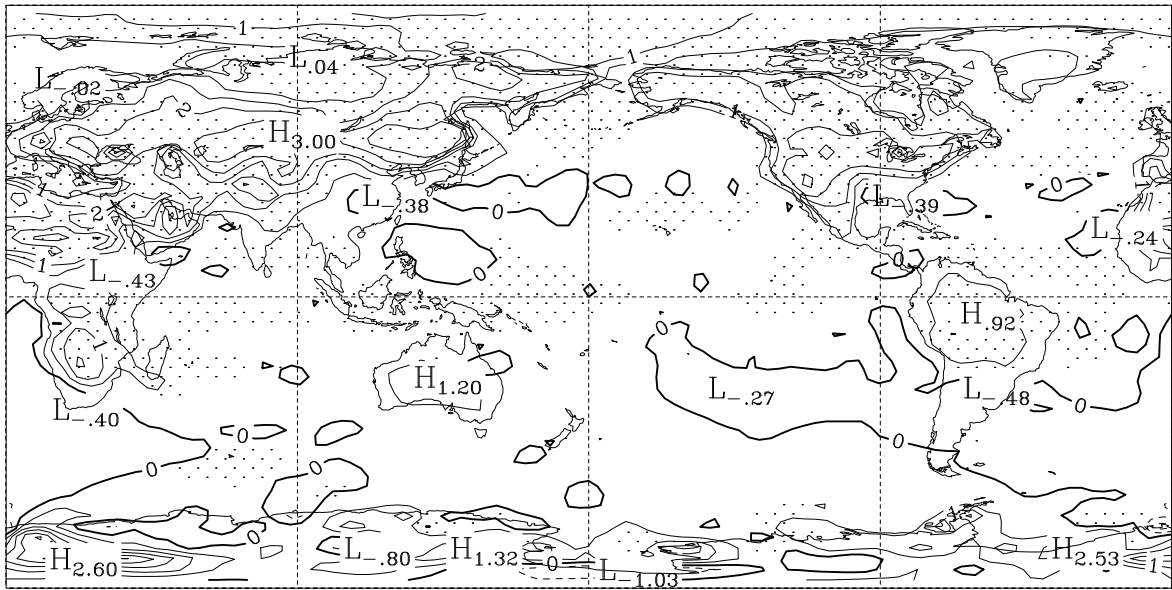
Dodson J.R. (ed.), 1992: The Naive lands: prehistory and environmental change in Australia and the south-west Pacific. *Longman Cheshire*. 258p.

Kershaw A.P., D'Costa D.M., McEwan Mason J.R.C. and Wagstaff B.E., 1991: Palynological evidence for Quaternary vegetation and environments of mainland south-eastern Australia. *Quaternary Science Reviews*, **10**, 391-404.

Kershaw P., Quilty P.G., David B., Van Huet S. and McMinn A., 2000: Paleobiogeography of the Quaternary of Australia. *Memoir of the Association of Australasian Paleontologists*, **23**, 471-516.



(a) DJF Surface air temperature anomaly (6ka - PD)



(b) JJA Surface air temperature anomaly (6ka - PD)

Figure 1: The distribution of the difference in the surface air temperature between the 6 ka simulation and that of the present day; a) DJF and b) JJA. Regions of statistical significance at the 95% level are stippled.

SURFACE TEMPERATURE AND HEAT FLUX VARIABILITY AND THEIR CHANGES WITH GLOBAL WARMING

Bin Yu and George J. Boer

Canadian Centre for Climate Modelling and Analysis, Meteorological Service of Canada

University of Victoria, PO Box 1700, Victoria, BC V8W 2Y2, Canada

Bin.Yu@ec.gc.ca; George.Boer@ec.gc.ca

1. INTRODUCTION

Sea surface temperature (SST) mediates the energy exchange at the air-sea interface and the variability of SST on different timescales reflects this coupling. This study analyzes the SST variability and its change with global warming. We directly relate the large-scale features of SST variability and heat flux (HF) variability based on both the NCEP/NCAR reanalyses and the results of the CCCma coupled atmosphere-ocean model.

2. DATA AND METHODOLOGY

The CCCma coupled model, control climate, forcing scenarios, and the simulated climate change are described in Flato et al.(2000) and Boer et al.(2000a,b). We use three 1000-yr model outputs, including the control run (CTRL) and two stabilization integrations with the forcing “stabilized” at year 2050 and 2100 values (referred to as STAB-2050 and STAB-2100, respectively). The NCEP/NCAR reanalyses monthly data, which cover the 50-yr period 1949-1998, are also employed (Kistler et al. 2001).

The energy balance of the upper layer of the ocean, after subtracting out climatological mean values of the terms, is

$\frac{C\{T_d'(t+\Delta t)-T_d'(t)\}}{\Delta t} = R' + B' + A'$. Where C is the oceanic heat capacity, T the surface temperature, R and B the radiative and turbulent energy exchanges across the surface, and A the convergence of heat in the layer by transport processes (Boer, 1993). The temperatures on the *lhs* of the equation are daily values while the *rhs* terms are monthly means. When the equation is squared and averaged, the *lhs* takes the form $\frac{2C^2}{\Delta t^2} \overline{T_d'^2\{1-r(\Delta t)\}}$ where r is the lagged autocorrelation. We connect the daily variability

to the variability of the monthly mean with the relationship $\overline{T'^2} = \frac{\overline{T_d'^2}}{\Delta t} (1+D)$ where $D = 2 \sum_{\tau=1}^{\Delta t} \left(1 - \frac{\tau}{\Delta t}\right) r(\tau)$ involves the lagged autocorrelations of daily values (von Storch and Zwiers, 1998). Thus the monthly mean temperature variance is related to the variance of forcing terms as

$$\overline{T'^2} = G(R' + B' + A')^2 \quad \text{or} \quad \sigma_T^2 = G(\sigma_R^2 + \sigma_B^2 + \sigma_A^2)e = G\sigma_o^2 e \quad (1)$$

where the transfer factor G depends on the autocorrelation structure of temperature, and σ_o^2 is the sum of the surface heat flux variances and the variance of oceanic heat flux convergence. σ_o^2 gives the contribution to the generation of temperature variance that would apply if the components were independent of one another, while e (the “efficiency” factor) measures the degree to which these physical forcing mechanisms act to counteract one another.

3. RESULTS

The surface energy budget from the control simulation is reasonably similar to observational estimates (Boer, 1993; Yu and Boer, 2002), although observation-based net HF and individual flux components still exhibit considerable differences (e.g. Trenberth et al., 2001). In some ways, the variability of HF is easier to estimate than the mean fluxes themselves. Systematic errors and biases in the means are of less importance and the main spatial scales of longer term variability tend to be large (WCRP, 2000). Figure 1 compares the results of SST variability and associated HF variability, based on (1), between CTRL and NCEP reanalyses. The qualitatively similar features are clear evident, though the modelled tropical variability is weak especially in the equatorial eastern Pacific. The configuration of σ_o^2 largely determines the SST variability. Nevertheless, it is important that the overall effect of $G*e$ also exhibits a spatial distribu-

tion bearing a resemblance to the spatial pattern of SST variability, indicating that they are not negligible contributors in determining the temperature variability.

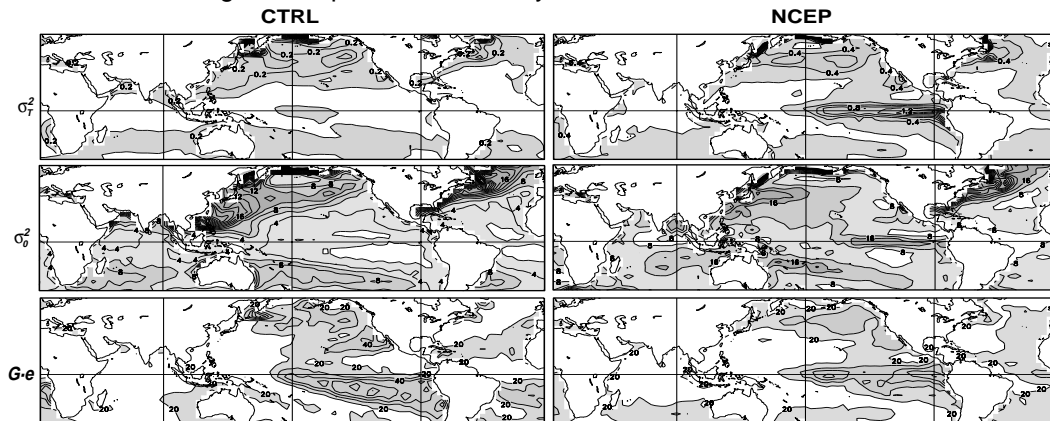


Figure1 Geographical distributions of SST variances (σ_T^2 , $^{\circ}\text{C}^2$), the total HF variances (σ_o^2 , $10^2\text{W}^2\text{m}^{-4}$), and $G*e$ ($10^{-50}\text{C}^2/\text{W}^2\text{m}^{-4}$) from the control simulation (CTRL) and NCEP reanalyses.

Figure 2 displays the percentage change of SST variability and variability budget terms with global warming, $\frac{\delta\sigma_T^2}{\sigma_T^2} = \frac{\delta\sigma_o^2}{\sigma_o^2} + \frac{\delta G}{G} + \frac{\delta e}{e}$. The temperature variances are generally reduced in the tropical Pacific and enhanced in the subtropical Pacific, while enhanced variability occupies most of the Atlantic ocean. The change in HF variance σ_o^2 explains much of SST variability change, although not all. There are notable differences between the changes of SST variability and that of σ_o^2 in the tropical central Pacific, the Indian ocean and mid-latitudes of the North Atlantic. In these regions, the SST variability decreases (increases) despite an increase (decrease) in σ_o^2 and either little change or even an increase in e . The changes are associated with the transfer factor G reflecting the temperature autocorrelation structure. In the tropics, SST has a shorter memory in the warming scenarios than that in the current climate, resulting in a decreasing of temperature persistence. In the mid-latitudes of the North Atlantic, on the other hand, the covariance relationships between HF are changing (negative covariances are decreasing) to produce a larger e relative to CTRL. The temperature persistence increases also in this area.

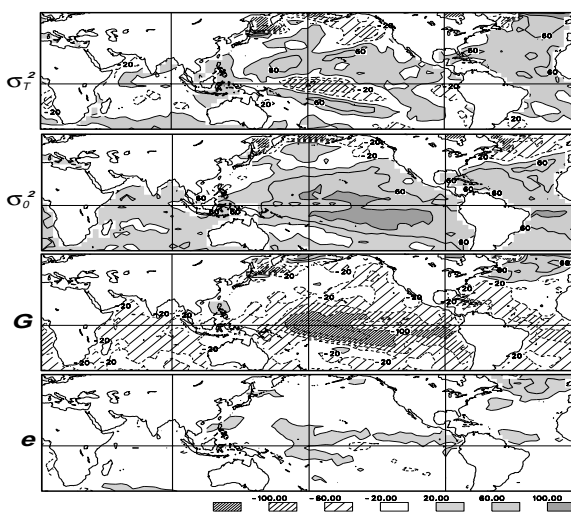


Figure 2 Percentage changes of SST variability with global warming (STAB-2100 relative to CTRL) and the associated variability balance.

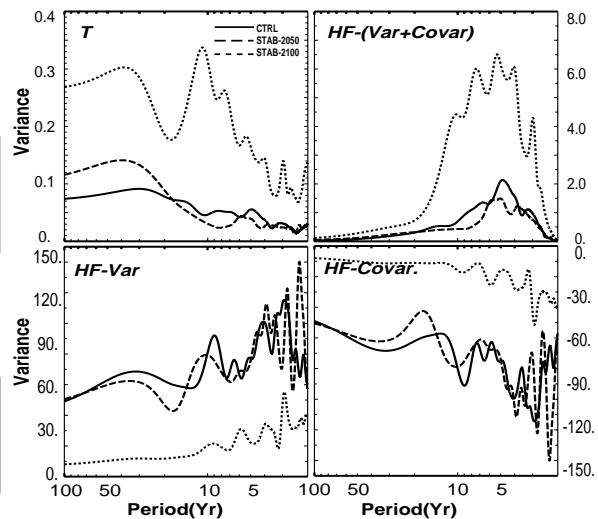


Figure 3 Power spectra of the regional mean SST, HF and HF covariances from the model integrations, including CTRL, STAB-2050 and STAB-2100.

A power spectrum analysis over the mid-latitudes (45-55°N) of the North Atlantic shows the relationship between temperature and HF variability in different timescales (Fig.3). In contrast to the increase of SST spectra, the spectra of the surface turbulent and ocean transport fluxes show significant decreases in the STAB-2100 warming scenario relative to the CTRL. This highlights again that it is the changes of HF covarinces rather than HF variances alone that are responsible for the changes of temperature variability.

4. SUMMARY

SST variance is expressed as a combination of three factors: the sum of the variances of surface radiative and turbulent fluxes and the ocean heat transport, a transfer factor representing the SST persistence, and an efficiency factor associated with the covariance relationship among these terms. The geographical distribution of SST variance follows that of the sum of the variances of the heat fluxes but modified by a term reflecting the SST autocorrelation structure and an efficiency factor reflecting the covariance structure among the heat fluxes.

The changes of SST variability with GHG-induced warming show broad-scale features, which become more prominent with the increase of the external forcing and on longer timescales. Changes in different components of (1) gave the change in SST variability in different geographical regions and each plays an important role.

References

- Boer, G.J., 1993, *Climate Dynamics*, 8, 225-239.
- Boer, G.J. et al., 2000a, *Climate Dynamics*, 16, 405-425.
- Boer, G.J. et al., 2000b, *Climate Dynamics*, 16, 427-450.
- Flato, G.M. et al., 2000, *Climate Dynamics*, 16, 451-467.
- Kistler, R. et al., 2001, *Bull AMS*, 82, 247-268.
- Trenberth, K.E. et al., 2001, *Climate Dynamics*, 17, 259-276.
- von Storch H., and F. Zwiers, 1998, Cambridge University Press, 494pp.
- WCRP, 2000, WCRP-112, 303pp.
- Yu, B., and G.J. Boer, 2002, *Climate Dynamics*, in press.